Article

Enhancer-associated aortic valve stenosis risk locus 1p21.2 alters NFATC2 binding site and promotes fibrogenesis

Arnaud Chignon, Mickael Rosa, Marie-Chloé Boulanger, ..., Sébastien Thériault, Yohan Bossé, Patrick Mathieu

patrick.mathieu@fmed.ulaval. ca

HIGHLIGHTS

1p21.2 risk locus is associated with calcific aortic valve stenosis

Rs6702619 is located in an enhancer including chromatin interaction with *PALMD*

Risk variant prevents the recruitment of NFATC2 lowering the expression of *PALMD*

Lower expression of PALMD promotes actin polymerization and a fibrogenic program

Article

Enhancer-associated aortic valve stenosis risk locus 1p21.2 alters NFATC2 binding site and promotes fibrogenesis

Arnaud Chignon,[1] Mickael Rosa,[1] Marie-Chloé Boulanger,[1] Déborah Argaud,[1] Romain Devillers,[1] Valentin Bon-Baret,[1] Ghada Mkannez,[1] Zhonglin Li,[1] Anne Rufiange,[1] Nathalie Gaudreault,[1] David Gosselin,[2] Sébastien Thériault,[3] Yohan Bossé,[2] and Patrick Mathieu[1,*]

SUMMARY

Genome-wide association studies for calcific aortic valve stenosis (CAVS) previously reported strong signal for noncoding variants at 1p21.2. Previous study using Mendelian randomization suggested that the locus controls the expression of _PALMD_ encoding Palmdelphin (PALMD). However, the molecular regulation at the locus and the impact of PALMD on the biology of the aortic valve is presently unknown. 3D genetic mapping and CRISPR activation identified rs6702619 as being located in a distant-acting enhancer, which controls the expression of _PALMD_. DNA-binding assay showed that the risk variant modified the DNA shape, which prevented the recruitment of NFATC2 and lowered the expression of _PALMD_. In co-expression network analysis, a module encompassing _PALMD_ was enriched in actin-based process. Mass spectrometry and functional assessment showed that PALMD is a regulator of actin polymerization. In turn, lower level of PALMD promoted the activation of myocardin-related transcription factor and fibrosis, a key pathobiological process underpinning CAVS.

INTRODUCTION

Calcific aortic valve stenosis (CAVS) is a highly prevalent heart valve disorder characterized by a fibrocalcific process (Lindman et al., 2016). There is no approved pharmacologic treatment for CAVS. For symptomatic patients in end-stage disease, the only therapeutic option is to replace the aortic valve (AV) by either surgical or trans-catheter approaches, which are associated with significant mortality/morbidity and elevated cost (Lindman et al., 2016). The identification of a molecular phenome (Koonin and Wolf, 2010) (i.e., gene regulation, expression, function) is thus a priority as it could lead to the development of novel noninvasive therapies to prevent or treat CAVS. The development of CAVS is a slow process, which relies on a progressive remodeling of the extracellular matrix (ECM) (Chen and Simmons, 2011). Mesenchymally derived valve interstitial cells (VICs) are typified by a high plasticity (Schlotter et al., 2018). VICs transition from quiescent into activated cells during tissue repair (Taylor et al., 2000). The acquisition of a secretory phenotype by activated VICs is one of the earliest feature involved in the pathogenesis of CAVS. Key underpinning molecular circuits that promote the activation of VICs leading to fibrosis and remodeling of the AV are largely unknown.

During the last several years, genome-wide association (GWA) studies have identified thousands of loci associated with diverse complex trait disorders (Welter et al., 2014). GWA and Mendelian randomization studies have contributed to identify causal drivers involved in different pathological conditions and in certain cases have fueled the development of novel therapies (Dewey et al., 2017). Hence, GWA-based approaches hold promise for the identification of molecular drivers involved in the pathogenesis of several complex trait disorders. However, as the vast majority of disease-associated variants reside in the noncoding genome, the identification of causal variants and their target genes remains a challenging task. Data have shown that noncoding variants with _cis_-regulatory activity are enriched in distant-acting enhancers. Recently, two independent GWA studies identified rs7543130 and rs6702619, which are both located on chromosome 1p21.2 and in perfect linkage disequilibrium (LD) ($r^2 = 1$), as being associated with CAVS at a genome-wide significance level (Helgadottir et al., 2018; Thériault et al., 2018). _Cis_-expression quantitative trait loci (eQTL) in AVs showed that the index variant, which is intergenic, is associated with the

[1]Laboratory of Cardiovascular Pathobiology, Quebec Heart and Lung Institute/Research Center, Department of Surgery, Laval University, 2725 Chemin Ste-Foy, G1V-4G5, Québec City, QC, Canada

[2]Department of Molecular Medicine, Laval University, Québec City, QC, Canada

[3]Department of Molecular Biology, Medical Biochemistry and Pathology, Laval University, Québec City, QC, Canada

*Correspondence: patrick.mathieu@fmed.ulaval.ca

https://doi.org/10.1016/j.isci.2021.102241
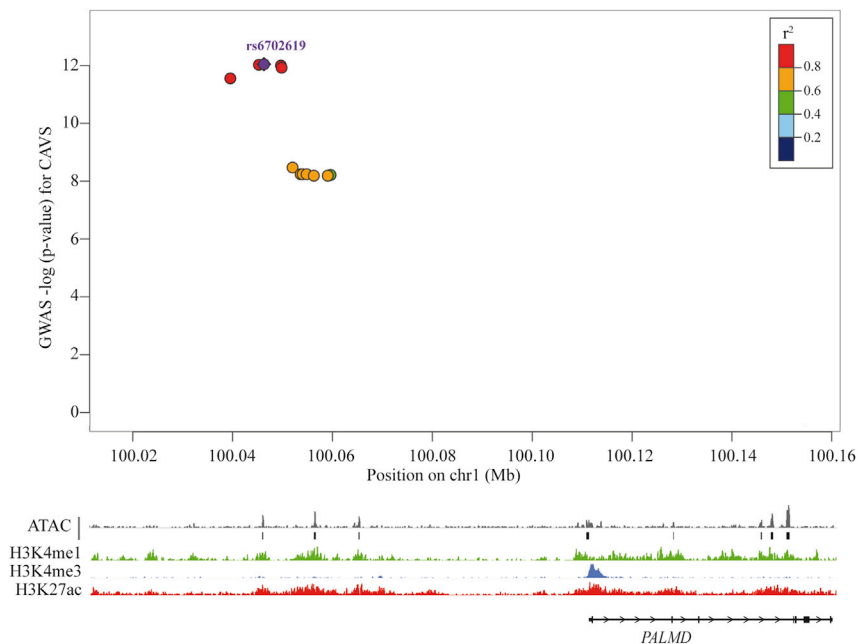
Figure 1. Variant rs6702619 is located in an enhancer controlling *PALMD* expression
The upper panel shows the genetic associations with CAVS surrounding rs6702619. The linkage disequilibrium (LD; r^2 values) for all SNPs with rs6702619 is indicated by colors. The bottom panel shows ATAC and ChIP-seq in human VICs.

expression of *PALMD* encoding Palmdelphin (PALMD) (Thériault et al., 2018). Mendelian randomization showed that lower expression of *PALMD* in AVs was causally associated with CAVS (Thériault et al., 2018). In the present work, mapping and functional characterization identified the 1p21.2 risk locus as an enhancer and showed that rs6702619 alters DNA shape and disrupts a transcription factor binding site (TFBS) for nuclear factor of activated T cells 2 (NFATC2/NFAT1). We identified PALMD as a regulator of actin polymerization. Lower expression of PALMD promoted the polymerization of actin, the activation of myocardin-related TF, the expression of smooth muscle α-ACTIN/*ACTA2,* and the development of a fibrogenic program, a key process in the development of CAVS.

RESULTS

Prioritization of noncoding gene variant at the *PALMD* risk locus

We previously performed Bayesian colocalization analysis by using a GWA meta-analysis for CAVS in QUEBEC-CAVS and UK Biobank (n = 2,359 cases, n = 350,060 controls) (Li et al., 2020) and eQTL data from 233 AVs. At the *PALMD* locus, the analysis revealed a strong posterior probability of shared signal between genetic association for CAVS and AV eQTL (PP4 = 0.997) (Li et al., 2020). Rs6702619, which is intergenic, was identified as the variant with the strongest associations with the GWA and valve eQTL. In VICs, an assay for transposase-accessible chromatin and sequencing (ATAC-seq) showed that rs6702619 and variants in strong LD were located in open chromatin (Figure 1). We next performed chromatin immunoprecipitation (ChIP) and DNA massively parallel sequencing (ChIP-seq) with an antibody directed against H3K4me1, an enhancer-associated histone mark. At the genome-wide scale, we detected 127,329 H3K4me1 peaks in VICs. Annotation of H3K4me1 peaks with GREAT (McLean et al., 2010) showed an enrichment in Gene Ontology (GO) for focal adhesions (FAs), cell-substrate adherens junction, actomyosin, and stress fibers (Table S1). At the 1p21.2 locus, which includes variants in strong LD (spanning ~10 kbp), the region encompasses enhancer-associated H3K4me1 peaks (Figure 1). In VICs, we performed a ChIP-seq for H3K27ac, which generated 82,662 peaks and showed that 1p21.2 has significant extended peaks for this mark and is thus compatible with the presence of active enhancers (Figure 1). Distant-acting enhancers are enriched in regulatory chromatin loops with promoters. In human primary VICs, we generated a genome-wide chromatin interaction map of enhancers and promoters by performing a H3K27ac HiChIP (Mumbach et al., 2016). Figure 2A shows the H3K27ac HiChIP interaction map of chromosome 1 and a close-up view with a resolution up to 5 kb. We implemented HOMER to identify high-confidence 3D
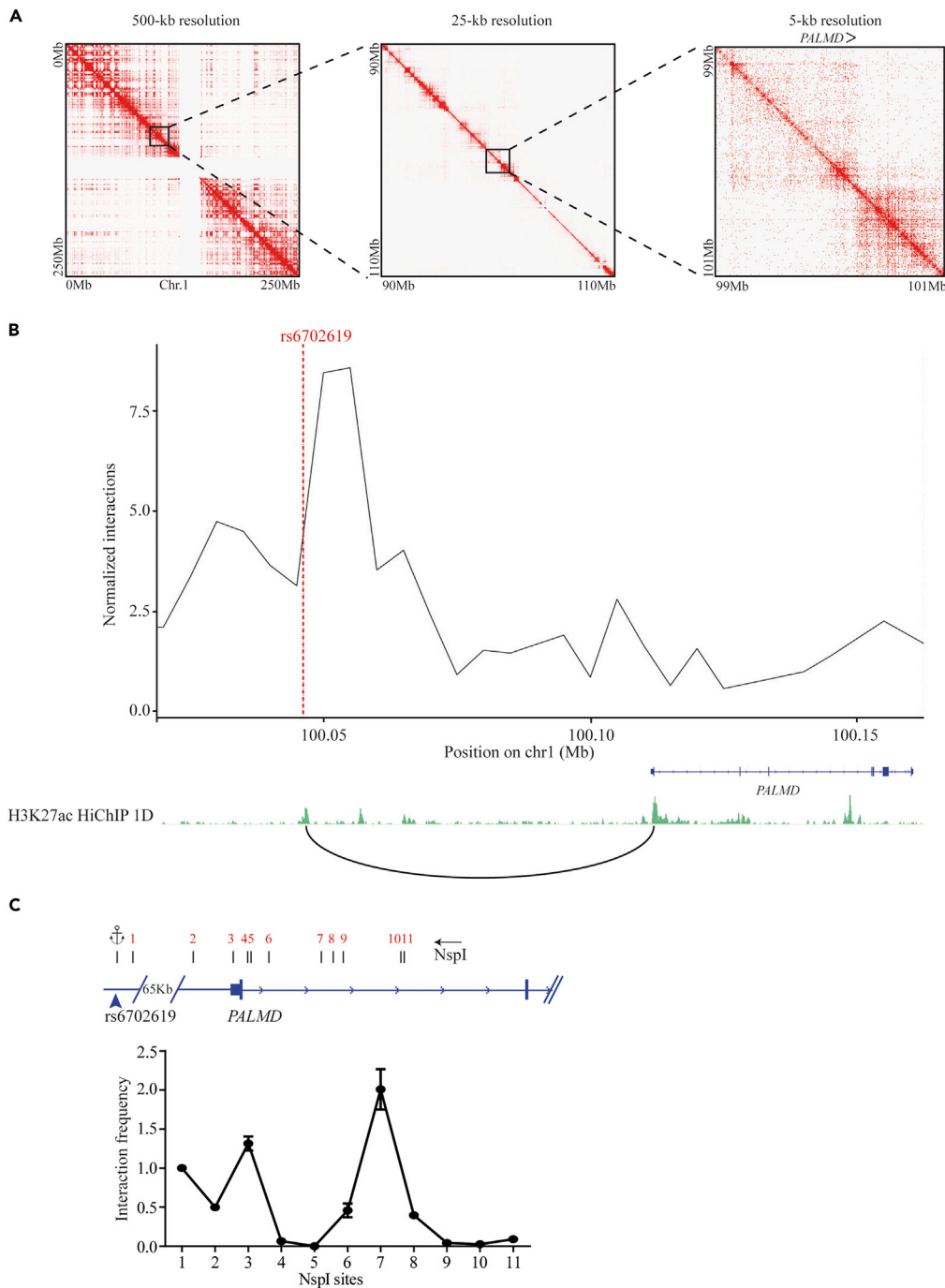
Figure 2. Variant rs6702619 connects with the promoter region of *PALMD*

(A) H3K27ac HiChIP contact matrix for VICs at 500-, 25-, and 5-kb resolutions.

(B) Virtual 4C analysis revealing contact between rs6702619 and *PALMD* promoter region; below are H3K27ac HiChIP 1D track and the arc representing significant normalized interaction identified by HOMER.

(C) NspI digestion pattern and chromosome conformation capture (3C) showing association between rs6702619 and *PALMD* promoter region.

interactions using a stringent false discovery rate (FDR) < 1×10^{-6}. We found that the region encompassing rs6702619 had significant chromatin interaction with the promoter region of *PALMD* distant from ~65 kb (Figure 2B). Data were next interrogated by using a virtual 4C analysis with a viewpoint as an anchor and

visualized in 2D (Mumbach et al., 2016). Virtual 4C with an anchor at rs6702619 provided a visualization of the interaction between the distant-acting enhancer and the promoter of *PALMD* (Figure 2B). These data were next confirmed by using a chromosome conformation capture assay (3C) using specific primers designed to ensure similar efficacy among the different primer sets covering the region (Table S2). A negative random ligation control with bacterial artificial chromosome (BAC) spanning the region (GRCh37/hg19 chr1: 99966146-100154958) showed that the primers did not detect significant signal (Table S3). Figure 2C shows 3C data in VICs anchored at rs6702619 and the significant interactions with the promoter region of *PALMD*. As another negative control, 3C and virtual 4C (using H3K27ac HiChIP) at the beta globin locus, which is not active in VICs, showed no significant interaction between the locus control region (LCR) (Krivega et al., 2015) and the globin genes (Figures S1A and S1B and Table S4). Hence, chromatin-associated marks and chromatin contact mapping suggest that the risk locus comprises an enhancer, which is spatially coordinated with the promoter of *PALMD*. Regulatory loci are often conserved in the genome. Among the different variants in LD, the only polymorphism showing a high degree of conservation is rs6702619 with PhastCons and PhyloP scores of 1 and 3.39, respectively (Table S5). To further prioritize noncoding gene variants in LD ($r^2 > 0.6$) with regulatory activity at the risk locus we performed an integrative weighted (IW)-scoring analysis (Wang et al., 2018), which combines functional annotations of 11 different scoring methods. IW-scoring identified rs6702619 as the most relevant functional variant (p = 0.009) (Table S6).

CRISPR activation at the rs6702619 promotes the expression of *PALMD*

Functional annotations and chromatin looping pattern suggest that rs6702619 has regulatory activity at the 1p21.2 risk locus. Figure S2A shows the topologically associated domain (TAD) in mesenchymal cells and centered on rs6702619. TADs, which are largely conserved between cell types, are compartments that promote and restrict chromatin looping within a submegabase domain (Dixon et al., 2012). This TAD includes *LPPR5*, *LPPR4*, and *FRRS1*, and the nearest gene to rs6702619 is *PALMD* (~65kb) (Figure S2A). To confirm that rs6702619 is within a regulatory region that exerts a control over the expression of *PALMD*, we used the clustered regularly interspersed short palindromic repeats (CRISPR)-mediated gene activation (CRISPRa) system (Figure 3A). Nuclease-deficient Cas9 (dCas9) was used to target the catalytic core of p300, a histone 3 lysine 27 acetyltransferase (H3K27ac) and positive regulator of enhancer/promoter activity, to the rs6702619 locus. Single guide RNA (sgRNA) targeting rs6702619 were cloned in a vector containing dCas9 fused with the catalytic core (amino acids 1048–1664) of p300. The control consisted in a vector containing identical target-specific sgRNA and a dCas9 fused with a catalytically inactive mutant p300 D1399Y. In VICs, the active vector dCas9-p300 increased the level of H3K27ac at the rs6702619 locus as shown by quantitative chromatin immunoprecipitation (Figure S2B). Compared with control dCas9-p300-D1399Y vector, the transfection of dCas9-p300 targeting rs6702619 in VICs increased the expression of *PALMD* by 1.3-fold (Figure 3B). Genes within 1 Mb from *PALMD* and sharing the same TAD were not modulated to a significant extent by CRISPRa at rs6702619 (Figure 3B). These data thus indicate that rs6702619 is functionally coordinated to *PALMD* and exerts a significant control over its expression in human VICs.

Risk variant rs6702619 disrupts a NFATC2 binding site

Cis-acting variants may impact gene expression by altering TF occupancy. Variants in strong LD ($r^2 > 0.9$) at the 1p21.2 risk locus were thus analyzed for their potential to alter TFBS by using an algorithm based on position weight matrix score (Kumar et al., 2017). Of the five variants in strong LD ($r^2 > 0.9$) only rs6702619 is included in a TF motif. The risk allele G at rs6702619 is within a core TFBS [5′-TT(T/G)TCCA-3′] for NFATC2, a TF involved in heart valve morphogenesis (Chang et al., 2004) (Figure 3C). Structural crystallographic data show that monomeric NFATC2 interacts with the major and minor grooves of DNA (PDB: 1OWR) (Figures 3D and S3). In the major groove, Q571 and Y424, which are in a loop of the Rel Homology Region (RHR) of the N-terminal portion of NFATC2, interact with AT base pair of the protective T allele at rs6702619 (Figures 3D and S3). Distribution of hydrogen bonds, which confer base-amino acid specificity, shows that glutamine (Q) has a preference for AT base pairs and thus substitution of T by G may affect the interaction with NFATC2 in the major groove ("base readout") (Luscombe et al., 2001). We next evaluated the effect of the risk variant on the predicted DNA shape (three-dimensional structure), an important feature for DNA-protein interaction, by using an experimentally validated algorithm (Rohs et al., 2009). Substitution of T by G at rs6702619 is predicted to modulate local DNA three-dimensional structure with lower degree in helical twist and increased minor groove width (Figures 3E and S4A). Side chain of a positively charged arginine residue (R537) in NFATC2 is projected in a narrow DNA minor groove of the consensus motif and provides electrostatic interaction (Figure 3D). Modeling and non-linear Poisson-Boltzmann calculations indicate that an increment in minor groove width, which is associated with the risk allele G, diminishes electronegativity and thus affects arginine-dependent electrostatic interaction and may alter the
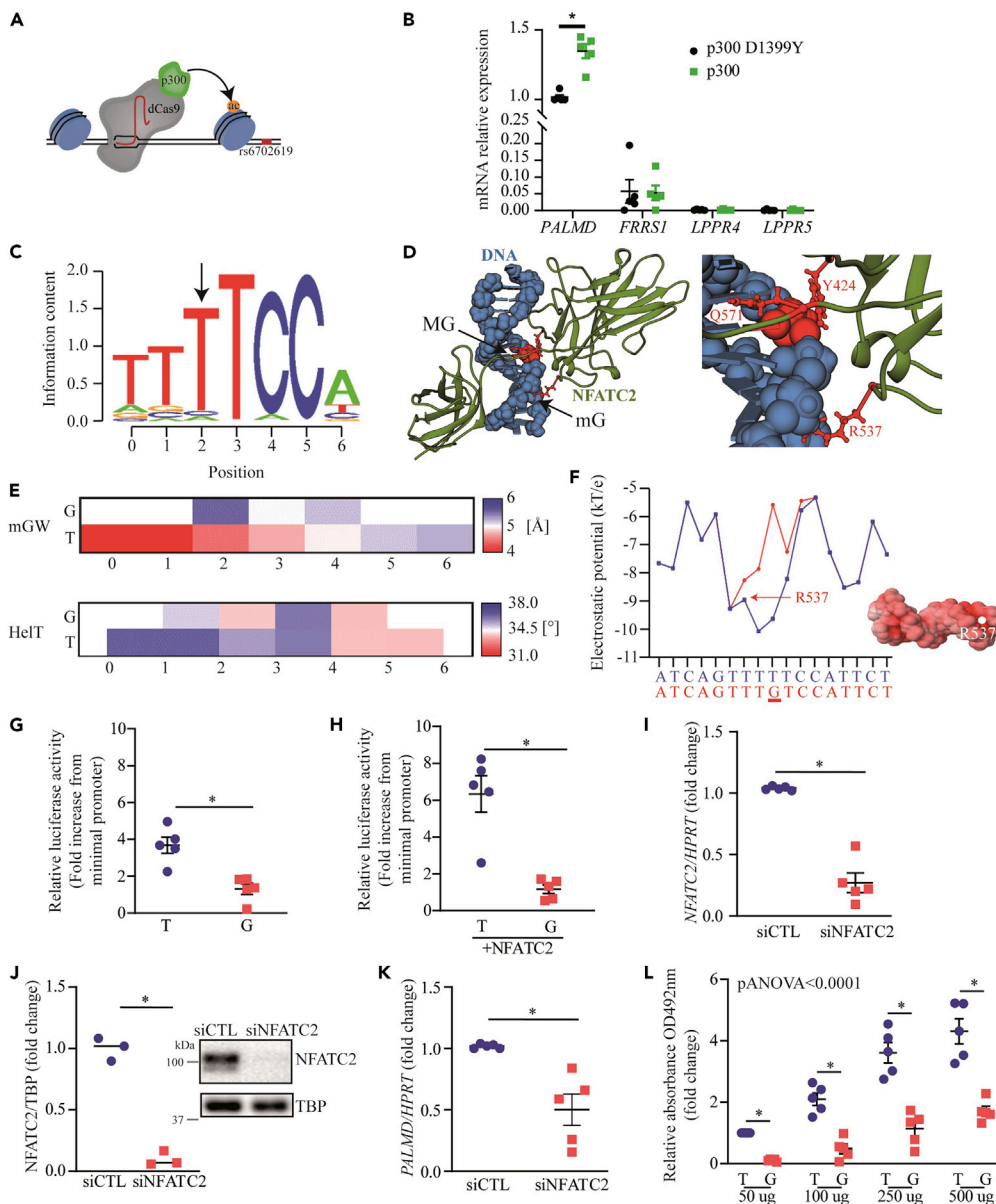
Figure 3. Impact of gene variant on NFATC2 binding

(A) Scheme showing dCas9 fused with the acetyltransferase p300 for epigenome editing.

(B) Expression of *PALMD*, *FRRS1*, *LPPR4*, and *LPPR5* in VICs in response to epigenome editing (n = 5); p300-D1399Y is the inactive mutant p300.

(C) Position-weighted matrix of NFATC2 binding site sequence. Arrow indicates rs6702619 base position where reference allele is T.

(D) Representation of NFATC2/DNA complex from crystallography data (MG: major groove, mG: minor groove). Right panel shows a close-up view of the interaction between NFATC2 amino acids and DNA bases.

(E) Minor groove width (MGW) and helical twist (HelT) parameters in the presence of T or G allele.

(F) Electrostatic potential of the minor groove in the presence of T or G allele. Red color intensity indicates negative electrostatic potential.

(G–L) (G and H) Luciferase reporter assay of enhancer constructions containing T or G allele (G) without and (H) with overexpression of NFATC2 (n = 5) normalized by the minimal promoter. (I) *NFATC2* mRNA (n = 5), (J) NFATC2 protein (n = 3), and (K) *PALMD* mRNA expression levels following NFATC2 siRNA knockdown (n = 5). (L) DNA-protein ELISA assay for NFATC2 interaction with 30-mer double-stranded oligonucleotides centered on rs6702619 and containing either the T or G allele (n = 5). Values are mean ± SEM, *p < 0.05. Statistical analyses, normal distribution testing: Shapiro-Wilk, (J) Wilcoxon-Mann-Whitney, (B, G–I, and K) Student's t test.

binding of NFATC2 ("shape readout") (Siggers and Gordân, 2014) (Figure 3F). Hence, the atomic resolution structure of NFATC2 with DNA indicates that the risk allele G alters base and shape readouts. This may significantly change the affinity and biological effect of NFATC2 (Yang et al., 2017). To substantiate the modeling derived from atomic-level data, we cloned a region of 500 bp centered on rs6702619 with a minimal promoter coupled to luciferase (see Figure S4B for the cloning details). Reporter vectors were transfected in human VICs. Compared with the minimal promoter, the reporter activity was increased by 3.5-fold in the construct containing the reference allele T (Figure 3G). In contrast, the vector containing the risk allele G decreased the reporter activity by 68% compared with the protective allele (Figure 3G). In addition, after normalization for the minimal promoter, the co-transfection of the enhancer reporter and NFATC2-encoding vectors showed that the activity of the protective T allele was increased by 5.9-fold compared with the risk allele (Figure 3H). These data suggested that NFATC2 is an important regulator of this locus and that risk allele G significantly reduces enhancer activity. To this effect, short interfering RNA (siRNA) for *NFATC2* in human VICs (Figures 3I and 3J) lowered the expression of *PALMD* by 37% (Figure 3K). Next, we performed a DNA-binding ELISA assay. Biotin-labeled 30-mer double-stranded oligonucleotides centered on rs6702619 were synthesized and linked to streptavidin-coated plates to assess the binding of NFATC2. This experiment showed that replacement of T by G at rs6702619 significantly lowered the binding affinity for NFATC2 between 60% and 89% (Figure 3L). Hence, the risk allele G at rs6702619 modifies a TFBS and negatively regulates the affinity for NFATC2, which leads to lower expression of *PALMD*.

Weighted gene co-expression network analysis

Gene variants and altered gene expression profile during CAVS are likely part of a larger network organization, which modifies biological responses. We performed an unbiased weighted gene co-expression network analysis (WGCNA) in 233 surgically explanted mineralized AVs from which transcriptome-wide expression data were generated (Thériault et al., 2018). A clustering dendrogram shows the 20 different modules of co-expression profile (Figure S4C). The red module includes 283 genes and encompasses *PALMD* (Table S7). As expected, several gene co-expression modules were significantly related to hemodynamic indices of CAVS severity (Figure 4A). Weighted co-expression of the *PALMD* module (red) was negatively and positively related to the peak trans-aortic gradient ($p = 1 \times 10^{-7}$) and the AV area ($p = 3 \times 10^{-4}$), respectively (Figure 4A). These data are consistent with the inverse relationship between the expression level of *PALMD* and CAVS risk. The *PALMD* (red) module has strong connection (adjacency) with the salmon module (Figure S4C), which encompasses 94 genes (Table S8). GO analysis showed that developmental pathways such as heart morphogenesis ($P_{adjusted} = 3.5 \times 10^{-4}$) and actin filament-based process ($P_{adjusted} = 9.7 \times 10^{-5}$) were enriched in the *PALMD* module (red) and were shared with the connected (salmon) module (Figure 4B and Table S9). These data thus suggest that *PALMD* is associated in diseased AVs with the reactivation of genes involved in developmental pathways, regulation of cell fate, and actin-dependent processes.

PALMD regulates cell shape and actin-based dynamics

To document the function of *PALMD* in VICs, we first evaluated its cellular distribution. Immunofluorescence in Triton-treated VICs showed that a significant amount of PALMD was co-distributed with F-actin (Figure S5A). Knockdown of *PALMD* with small interfering RNA (siRNA), which lowered the mRNA and protein levels (Figure 5A), revealed a striking modification in cell shape. siRNA-treated VICs had higher cell area and lower length/width ratio, indicating a major function for PALMD to control cell shape (Figures 5B and 5C) (see Figure S5B for a wide field view). Phalloidin staining of F-actin showed that VICs with a knockdown of *PALMD* had strong stress fibers (Figure 5D). Quantification showed a significant increase of F-actin area per cell after a knockdown of PALMD (Figure 5E). FAs are dynamic and active structures, which are co-regulated with actin stress fibers. We thus quantified FAs in response to PALMD modulation. In VICs, siRNA-mediated knockdown of PALMD increased the number of FAs (as shown by immunofluorescence for vinculin) by 3-fold (Figures 5F and 5G). Taken together, these data suggest that PALMD controls in VICs the dynamic of actin and FAs, which could thus modify signaling and gene expression.

PALMD regulates fibrogenesis

As modification of actin dynamics is linked to cell activation, we measured the level of *ACTA2*, a marker of VIC activation with a secretory phenotype and considered as an early marker in the development of CAVS (Rutkovskiy et al., 2017). In VICs, after a knockdown of PALMD, the mRNA and protein levels of *ACTA2*/α-ACTIN increased by 1.5- and 1.3-fold respectively (Figures 6A and 6B). In line with this finding, we documented that siRNA-mediated knockdown of PALMD also increased the mRNA levels for *TGFB2*, *COL1A2*, *MMP2,* and *MMP9* (Figures 6C–6F). These findings suggested that PALMD regulates tissue remodeling and fibrogenesis, a process involved in the development of CAVS. To buttress these findings we measured the
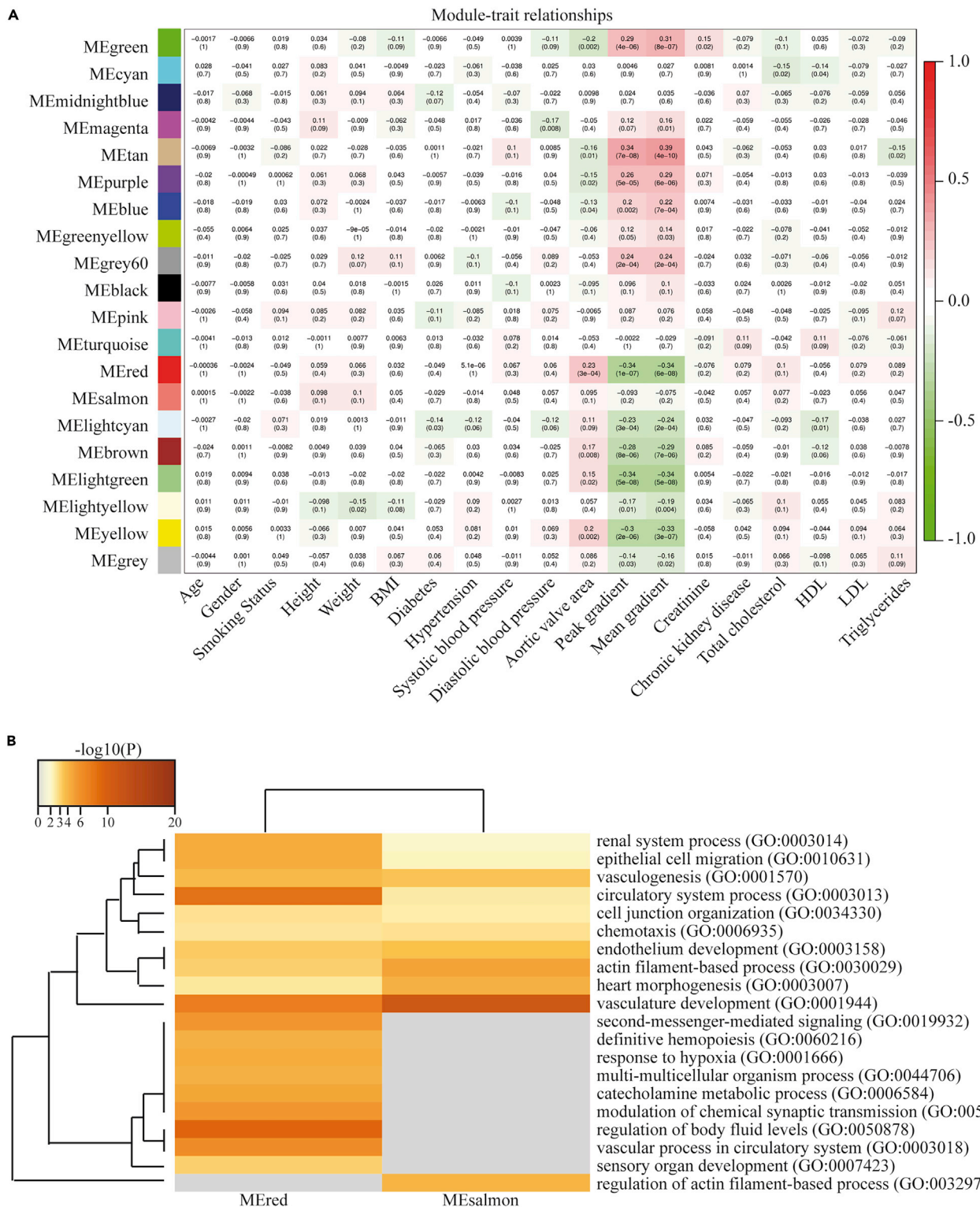
Figure 4. Weighted gene co-expression network and relationships with biological and clinical data
(A) Module-trait relationships for WGCNA in 233 calcified aortic valves.
(B) GO analysis for the red (MEred) (includes PALMD) and salmon (MEsalmon) modules.
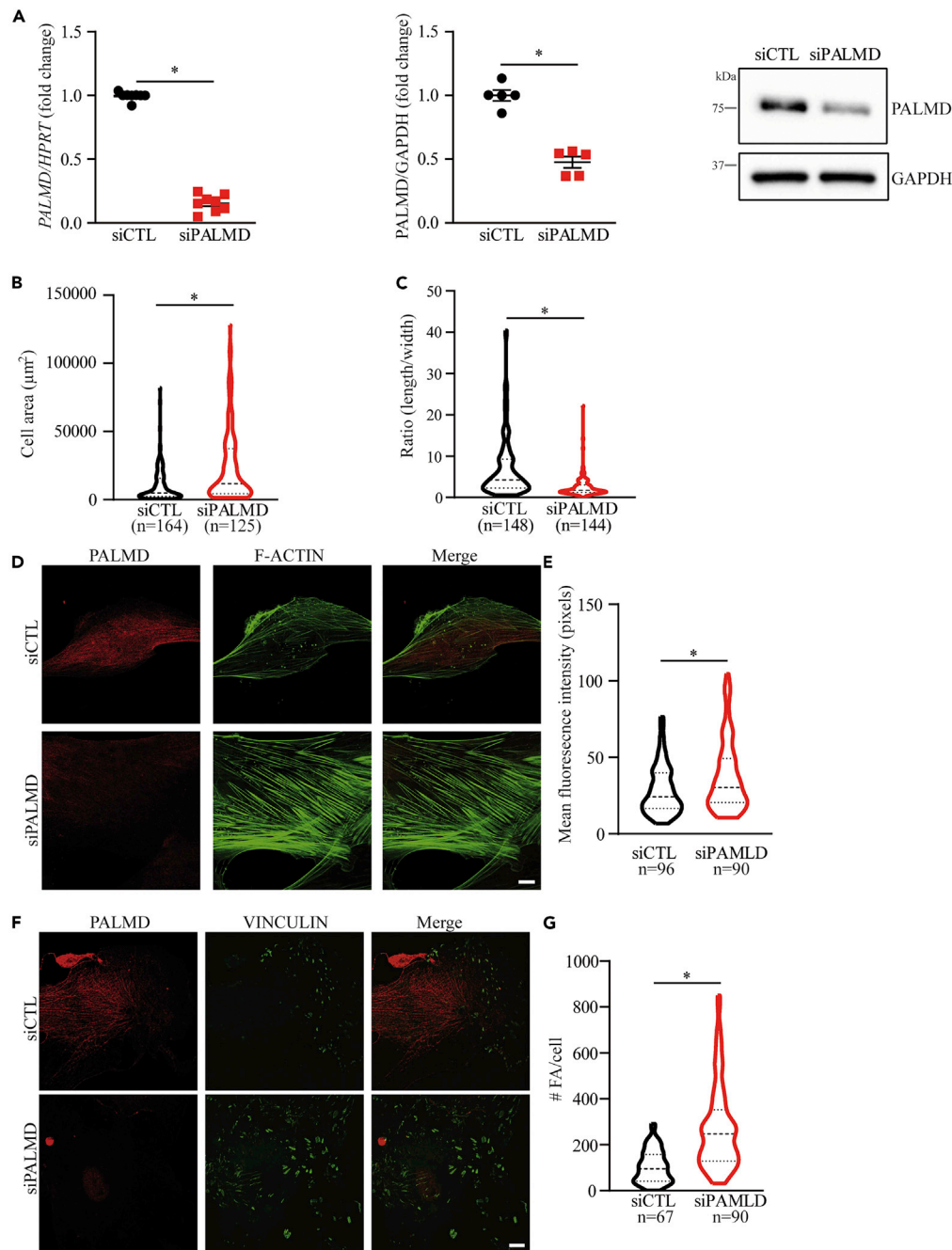
Figure 5. PALMD levels affect VICs morphology

(A–G) siRNA-mediated knockdown of PALMD on (A) mRNA (n = 8) and protein levels (n = 5), (B) cell area, (C) length/width ratio, (D and E) F-actin polymerization (n = 4), and (F and G) focal adhesion formation (vinculin) (n = 3). Scale bars, 10 μm. Values are mean ± SEM. *p < 0.05. Statistical analyses, normal distribution testing: Shapiro-Wilk, (B, C, E, and G) Wilcoxon-Mann-Whitney, (A) Student's t test.

protein level of collagen type I, a predominant collagen in the AV and highly expressed in surgically explanted mineralized AVs (Hutson et al., 2016). In VICs, the knockdown of PALMD for 72 h increased the synthesis of collagen type 1 by 1.3-fold (Figure 6G). The expression of *COL1A2, MMP9,* and *TGFB2* is under the regulation of serum response factor (SRF) and myocardin-related transcription factors (MRTFs) (Gilles et al., 2009; Haak et al., 2014; Kuzniewska et al., 2013; Li et al., 2012). MRTFs contain an N-terminal RPEL domain by which they interact with G actin. During the polymerization of actin, reduced G actin pool contributes to
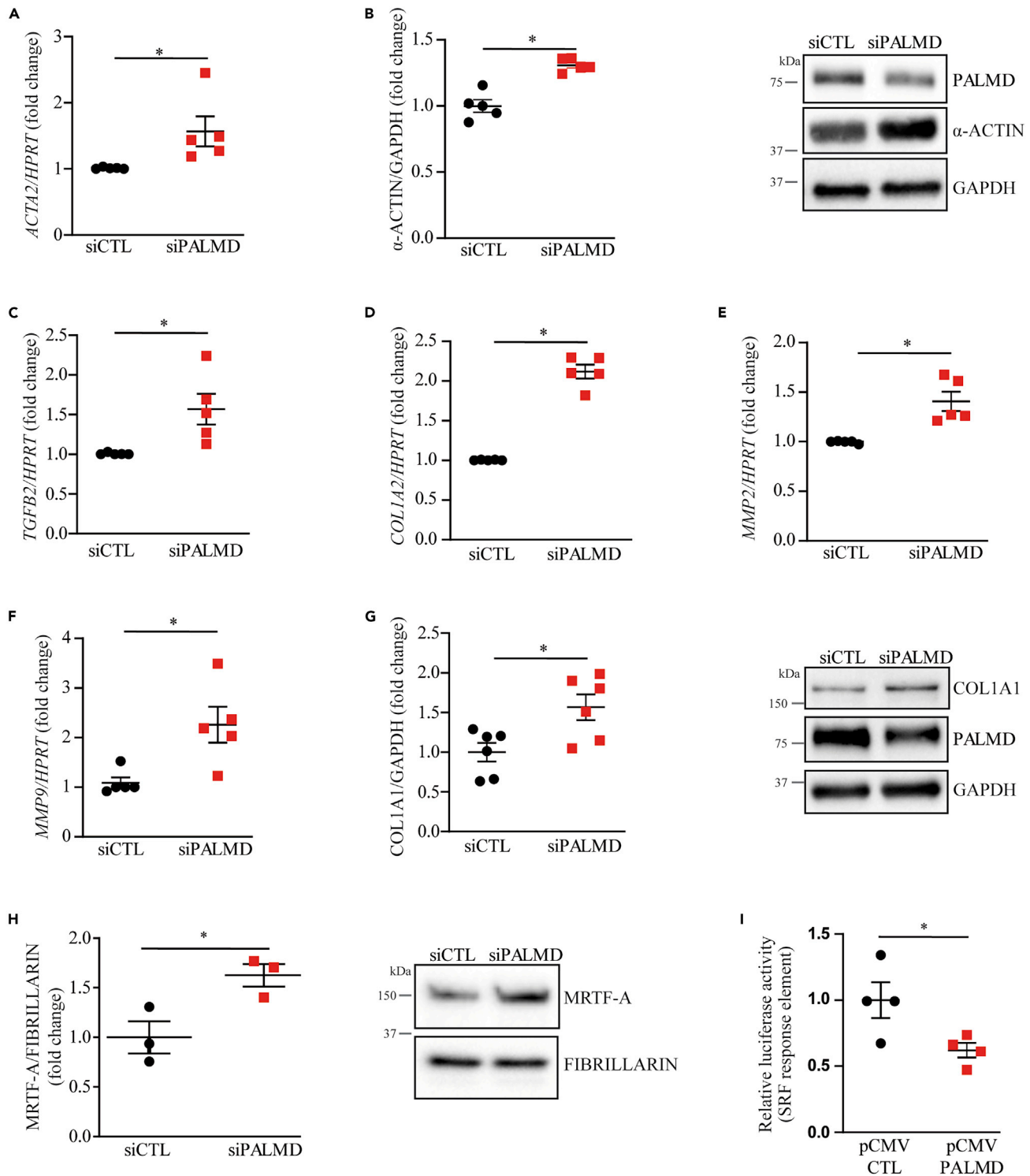
Figure 6. Lowering PALMD induces fibrogenesis

(A–H) siRNA-mediated knockdown of PALMD on (A) *ACTA2*/α-ACTIN mRNA and (B) protein levels; (C) *TGFB2*, (D) *COL1A2*, (E) *MMP2*, and (F) *MMP9* mRNA levels (n = 5); (G) COL1A1 protein expression (n = 6); and (H) MRTF-A nuclear localization (n = 3).

(I) SRF response element luciferase reporter assay (n = 4). Values are mean ± SEM, *p < 0.05. Statistical analyses, normal distribution testing: Shapiro-Wilk, (A and C–F) Wilcoxon-Mann-Whitney, (B and G–I) Student's t test.

release MRTFs, which translocate to the nucleus and act as cofactors for SRF. Thus, we reasoned that a lower expression of PALMD may activate the nuclear translocation of MRTF-A (also known as MKL1 or MAL). In isolated VICs, 24 h after the transfection with an siRNA-targeting PALMD, we observed a significant rise of MRTF-A in nuclear extracts (Figure 6H). In a reporter assay for SRF response elements conducted in COS-7, which do not express appreciable level of PALMD (Figure S5C), we evaluated the response to a vector expressing PALMD. Consistently, this assay showed that the overexpression of PALMD in COS-7 reduced by 38% the SRF reporter activity (Figure 6I). These data thus underlined that PALMD regulates the MRTF-SRF pathway.

PALMD is a regulator of actin polymerization

PALMD is a member of the paralemmin family and evolved in vertebrates from gene duplication events (Hultqvist et al., 2012). Analysis of amino acid sequence in different vertebrate species (Dereeper et al., 2008) indicates that PALMD is highly conserved, especially among the mammalian clades (Figure S5D). Hence, considering its localization in the cytosol and its evolutionary conservation, we hypothesized that PALMD has important regulatory functions, which may be shaped by its interactome. We examined the protein interactome of PALMD by using liquid chromatography-tandem mass spectrometry (LC-MS/MS). A vector encoding for hemagglutinin (HA)-PALMD was transfected in HEK293T and immunoprecipitated for subsequent LC-MS/MS assay. This analysis showed that PALMD may interact with up to 595 proteins (Tables S10 and S11). The protein interactome was enriched in GO for cell adhesion, structural molecule activity, and actin-dependent ATPase activity (Figure 7A and Table S12). Among the different proteins, actin was among the strongest hits. This interaction was verified in co-immunoprecipitation experiments. In VICs, the pull down of native PALMD recovered α-ACTIN confirming data obtained in mass spectrometry (Figure 7B). Conversely, the immunoprecipitation of native α-ACTIN in VICs also recovered PALMD (Figure 7C). *In situ* proximity ligation assay was also performed to spatially locate the intracellular interactions between PALMD and α-ACTIN. In isolated VICs, we found that PALMD interacted with α-ACTIN in the cytosol (Figure 7D). Next, we used a blot overlay assay to evaluate the interaction of PALMD with actin. F- and G-actin were immobilized on nitrocellulose membranes, which were incubated with cell extracts transfected with a vector encoding for HA-PALMD. The interactions were detected with an anti-HA antibody. Both G and F actin interacted with PALMD (Figure 7E). Having shown that PALMD is a protein that interacts with actin, we reasoned that it could regulate the polymerization process. We thus tested recombinant PALMD in actin polymerization assay with fluorescent pyrene. In this assay, we found that PALMD dose-dependently and negatively impacted the polymerization of actin (Figure 7F). PALMD decreased the area under the curve of the polymerization assay by up to 37% (Figure 7G). These data thus indicate that PALMD is an actin binding partner and negative regulator of the polymerization process.

DISCUSSION

In this work, mapping and fine-grained molecular analyses of the 1p21.2 CAVS risk locus revealed that the risk variant rs6702619 is located in an enhancer region within a core TFBS for NFATC2. Atomic resolution data indicate that the risk allele G modifies target recognition and DNA shape, which impair the binding of NFATC2, a TF with key regulatory function in the AV (Chang et al., 2004). Functional assessment showed that PALMD is a regulator of actin polymerization. In turn, genetically determined lower expression of PALMD promotes MRFT/SRF-mediated gene expression and activation of VICs toward myofibroblast-like cells, an early process involved in the development of CAVS (Figure 7H).

Recently, GWA studies identified 1p21.2 as a risk locus for CAVS (Helgadottir et al., 2018; Thériault et al., 2018). Herein, by using fine mapping and functional assessment we provide evidence that rs6702619 is causally associated with the expression of *PALMD*. The index variant rs6702619 and SNPs in LD reside in an enhancer and may thus play a critical role in the cell identity and fate of VICs. By using CRISPRa, we underscored that the risk locus is mainly involved in the regulation of *PALMD*, whereas other genes sharing the same TAD are not. These data are in line with chromatin contact mapping, which showed spatial coordination between the risk locus and *PALMD*. Growing evidence suggests that noncoding variants may affect protein-DNA interactions by altering local atomic structure (Rohs et al., 2009). Analysis of atomic-level data revealed that the risk variant alters significantly both base-readout and DNA shape, which could affect the binding of NFATC2. Our data showed in DNA-binding ELISA assay that the risk variant significantly decreased the occupancy of NFATC2, suggesting a functional implication for this TF. To this effect, in VICs, the knockdown of NFATC2 significantly lowered the expression of *PALMD*. NFATC2 is a key regulator of heart valve biology and morphogenesis (Chang et al., 2004); Nfatc2 deficiency in mice results in

Figure 7. PALMD interacts with actin and regulates its polymerization

(A) Gene ontology (GO) terms enriched for PALMD protein interactome.

(B and C) PALMD and α-ACTIN co-immunoprecipitation (n = 3).
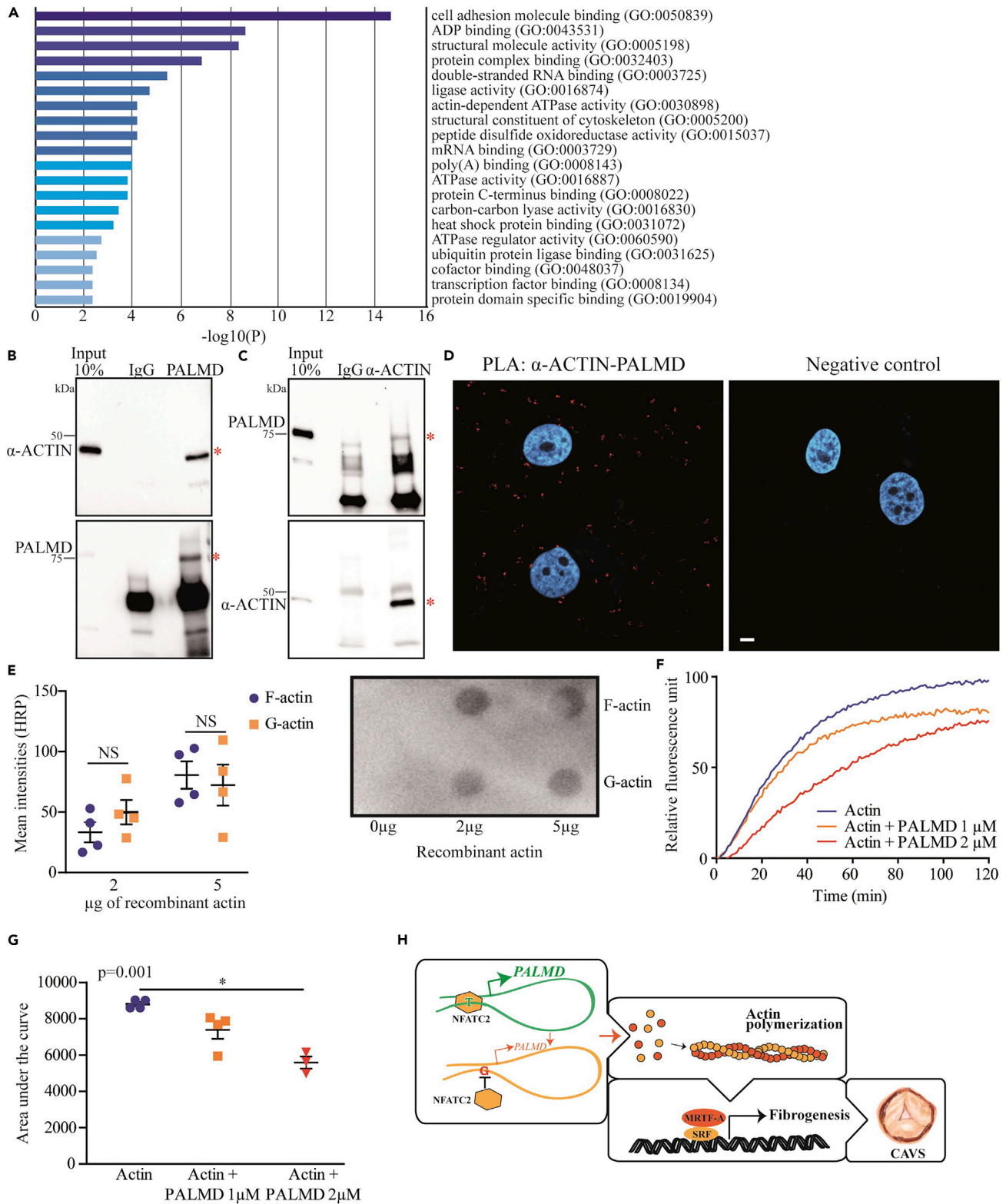
Figure 7. *Continued*

(D) Proximity ligation assay for PALMD and α-ACTIN (n = 2).

(E) Blot overlay assay of F- and G-actin interaction with PALMD (n = 4) by using various quantities of recombinant actin.

(F and G) Actin polymerization in the presence of PALMD 1 μM (n = 4) or 2 μM (n = 3) and area under curve of actin polymerization profiles.

(H) The G allele at rs6702619 hinders NFATC2 binding to the enhancer, resulting in decreased *PALMD* transcription. Reduced PALMD level in VICs leads to increased actin polymerization, enhancing MRTF-A nuclear translocation. MRTF-A/SRF binding to DNA response element initiates VICs activation toward myofibroblast-like cells, which promotes CAVS development. Scale bars, 10 μm. Values are mean ± SEM, *p < 0.05. Statistical analyses, normal distribution testing: Shapiro-Wilk, (E and G) Wilcoxon-Mann-Whitney.

lethal defects due to developmental abnormalities of cardiac valves and septa (de la Pompa et al., 1998; Ranger et al., 1998). Hence, disruption of TFBS and lower NFATC2 occupancy at 1p21.2 is a key process in lowering the expression of *PALMD*.

Previous work conducted in myocytes underlined that PALMD regulates cell shape (Nie et al., 2017). However, the molecular process whereby PALMD affects cell shape and dynamics was largely unknown until now. In isolated human primary VICs, we found that lower level of PALMD led to increased cell area. Moreover, we found that this cell modification was coordinated with higher level of FAs and expression of *ACTA2*/α-ACTIN, a marker of myofibroblasts. Data have consistently shown that transition of VICs into myofibroblast-like cells was an early process in the development of CAVS (Latif et al., 2015; Schlotter et al., 2018; Taylor et al., 2000). It is worth pointing out that myofibroblastic transformation of VICs following a knockdown of PALMD was accompanied by higher expression of genes involved in matrix remodeling such as *TGFB2*, *MMP9*, *MMP2*, and *COL1A2*. Also, lower level of PALMD in VICs was conducive to higher production of collagen type I, a major component of the ECM in AV and contributor to the remodeling process during CAVS. These data are in agreement with previous work showing that increased synthesis of collagen and production of ECM are among the key processes leading to valve thickening during CAVS (Hutson et al., 2016).

In the present work, LC-MS/MS data and immunoprecipitation in human VICs have identified PALMD as a protein that interacts with actin. Actin is highly conserved and interacts with a large number of proteins (Dominguez and Holmes, 2011). Numerous proteins thus fine-tune the complex process of actin polymerization as it is involved in a myriad of cellular functions (Davidson and Wood, 2016). Noteworthy, the present findings indicate that PALMD is a direct regulator of actin polymerization. In isolated cells, proximity ligation assay showed cytosolic interaction of PALMD with actin. *In vitro*, PALMD is a potent negative regulator of actin polymerization. In isolated cells, the knockdown of PALMD promoted the formation of F-actin. Hence, lower expression of PALMD, which dynamically and negatively regulates the polymerization of actin, promotes cell activation and a fibrotic gene program that relies on SRF-MRTF-A. To this effect, we observed an increased and significant nuclear translocation of MRTF-A in cells with a knockdown of PALMD. Consistently, SRF-dependent genes such as *TGFB2*, *MMP9*, and *COL1A2* were also overexpressed in cells with a knockdown of PALMD (Gilles et al., 2009; Haak et al., 2014; Kuzniewska et al., 2013; Li et al., 2012).

This study has several important clinical implications as previous work suggested, by using Mendelian randomization, a causal role for a lower expression of PALMD in CAVS (Thériault et al., 2018). The identification of PALMD as a new regulator of actin dynamics and polymerization in VICs provides substantive evidence for a major function of PALMD in the biology of the AV. In addition to CAVS, a GWA study also found at a genome-wide significance level an association between rs6702619 and aortic root diameter (Wild et al., 2017). This association has a directional effect that is concordant with CAVS risk. Hence, the aortic root and the AV, which share embryologic and developmental pathways, are under the regulation of this locus. Of note, the 1p21.2 locus is not, however, associated with coronary artery disease risk (van der Harst and Verweij, 2018). Clinically, the present findings may foster the development of therapies, which could be based on the biology of PALMD and its signaling pathway.

Noncoding risk variant at 1p21.2 modifies a TFBS for NFATC2. In turn, the activity of a distant-acting regulatory element residing in an enhancer is substantially impacted and it lowers the expression of PALMD. Genetically determined lower level of *PALMD* promotes the activation of VICs and fibrogenesis, an early pathogenic process in the development of CAVS. Hence, comprehensive assessment of the 1p21.2 risk locus provides a detailed map for the functional and molecular genetics in CAVS. These findings pave the way for further research, which may lead to therapies.

Limitations of the study

The impact of CRISPRa on the expression of *PALMD* was limited in human VICs as these primary cells were largely resistant to selection exhibiting a high level of mortality. The expression was determined on bulk non-selected transfected cells. It is thus expected that the effect of CRISPRa on the expression would be much higher if cells could have been selected. The process whereby PALMD regulates the polymerization of actin and activates an MRTF-SRF pathway was determined in isolated cells. Further work *in vivo* should be performed to investigate the contribution of PALMD to the fibrogenesis of the AV.

Resource availability

Lead contact

Further information and requests for resources should be directed to and will be fulfilled by the lead contact, Patrick Mathieu (patrick.mathieu@fmed.ulaval.ca).

Materials availability

Plasmids generated in this study are available on request.

Data and code availability

Raw data for ChIP-Seq, ATAC-seq, and HiChIP are available in the NCBI's Gene Expression Omnibus (GEO) repository (GSE154513).

METHODS

All methods can be found in the accompanying Transparent methods supplemental file.

SUPPLEMENTAL INFORMATION

Supplemental information can be found online at https://doi.org/10.1016/j.isci.2021.102241.

AUTHOR CONTRIBUTIONS

A.C., M.R., M.-C.B, and P.M. conceived and designed experiments. A.C. performed 3C experiments. A.C. performed HiChIP. A.C. conducted analyses for HiChIP data. A.C., D.A., and G.M. performed ChIP experiments. A.C., V.B.-B., and Z.L. conducted analyses of ChIP-seq data. *In silico* analyses were performed by A.C., M.R., and P.M. Cell culture, CRISPRa, qPCR, and western blots were performed by M.R., A.C., and M.-C.B. LC/MS/MS experiments was conducted by M.R. DNA binding ELISA assay was performed by R.D. Immunoprecipitation experiments were performed by R.D. and M.-C.B. WGCNA was performed by Y.B. Microscopy and immunofluorescence experiments were conducted by M.R. and M.-C.B. Reporter assays were performed by D.A. The actin polymerization assay was conducted by M.R. P.M., A.C., and M.R. drafted the manuscript. All the authors critically reviewed the manuscript and provided intellectual inputs.

DECLARATION OF INTERESTS

None.

REFERENCES

Chang, C.-P., Neilson, J.R., Bayle, J.H., Gestwicki, J.E., Kuo, A., Stankunas, K., Graef, I.A., and Crabtree, G.R. (2004). A field of myocardial-endocardial NFAT signaling underlies heart valve morphogenesis. Cell 118, 649–663.

Chen, J.-H., and Simmons, C.A. (2011). Cell-matrix interactions in the pathobiology of calcific aortic valve disease: critical roles for matricellular, matricrine, and matrix mechanics cues. Circ. Res. 108, 1510–1524.

Davidson, A.J., and Wood, W. (2016). Unravelling the actin cytoskeleton: a new competitive edge? Trends Cell Biol. 26, 569–576.

Dereeper, A., Guignon, V., Blanc, G., Audic, S., Buffet, S., Chevenet, F., Dufayard, J.-F., Guindon, S., Lefort, V., Lescot, M., et al. (2008). Phylogeny.fr: robust phylogenetic analysis for the non-specialist. Nucleic Acids Res. 36, W465–W469.

Dewey, F.E., Gusarova, V., Dunbar, R.L., O'Dushlaine, C., Schurmann, C., Gottesman, O., McCarthy, S., Van Hout, C.V., Bruse, S., Dansky, H.M., et al. (2017). Genetic and pharmacologic inactivation of angptl3 and cardiovascular disease. N. Engl. J. Med. 377, 211–221.

Dixon, J.R., Selvaraj, S., Yue, F., Kim, A., Li, Y., Shen, Y., Hu, M., Liu, J.S., and Ren, B. (2012). Topological domains in mammalian genomes identified by analysis of chromatin interactions. Nature 485, 376–380.

Dominguez, R., and Holmes, K.C. (2011). Actin structure and function. Annu. Rev. Biophys. 40, 169–186.

Gilles, L., Bluteau, D., Boukour, S., Chang, Y., Zhang, Y., Robert, T., Dessen, P., Debili, N., Bernard, O.A., Vainchenker, W., et al. (2009). MAL/SRF complex is involved in platelet formation and megakaryocyte migration by regulating MYL9 (MLC2) and MMP9. Blood 114, 4221–4232.

Haak, A.J., Tsou, P.-S., Amin, M.A., Ruth, J.H., Campbell, P., Fox, D.A., Khanna, D., Larsen, S.D., and Neubig, R.R. (2014). Targeting the myofibroblast genetic switch: inhibitors of myocardin-related transcription factor/serum response factor-regulated gene transcription prevent fibrosis in a murine model of skin injury. J. Pharmacol. Exp. Ther. 349, 480–486.

van der Harst, P., and Verweij, N. (2018). Identification of 64 novel genetic loci provides an expanded view on the genetic architecture of coronary artery disease. Circ. Res. 122, 433–443.

Helgadottir, A., Thorleifsson, G., Gretarsdottir, S., Stefansson, O.A., Tragante, V., Thorolfsdottir, R.B., Jonsdottir, I., Bjornsson, T., Steinthorsdottir, V., Verweij, N., et al. (2018). Genome-wide analysis yields new loci associating with aortic valve stenosis. Nat. Commun. 9, 987.

Hultqvist, G., Ocampo Daza, D., Larhammar, D., and Kilimann, M.W. (2012). Evolution of the vertebrate paralemmin gene family: ancient origin of gene duplicates suggests distinct functions. PLoS One 7, e41850.

Hutson, H.N., Marohl, T., Anderson, M., Eliceiri, K., Campagnola, P., and Masters, K.S. (2016). Calcific aortic valve disease is associated with layer-specific alterations in collagen architecture. PLoS One 11, e0163858.

Koonin, E.V., and Wolf, Y.I. (2010). Constraints and plasticity in genome and molecular-phenome evolution. Nat. Rev. Genet. 11, 487–498.

Krivega, I., Byrnes, C., de Vasconcellos, J., Lee, Y., Kaushal, M., Dean, A., and Miller, J. (2015). Inhibition of G9a methyltransferase stimulates fetal hemoglobin production by facilitating LCR/-globin looping. Blood 126, 665–672.

Kumar, S., Ambrosini, G., and Bucher, P. (2017). SNP2TFBS - a database of regulatory SNPs affecting predicted transcription factor binding site affinity. Nucleic Acids Res. 45, D139–D144.

Kuzniewska, B., Rejmak, E., Malik, A.R., Jaworski, J., Kaczmarek, L., and Kalita, K. (2013). Brain-derived neurotrophic factor induces matrix metalloproteinase 9 expression in neurons via the serum response factor/c-Fos pathway. Mol. Cell. Biol. 33, 2149–2162.

Latif, N., Quillon, A., Sarathchandra, P., McCormack, A., Lozanoski, A., Yacoub, M.H., and Chester, A.H. (2015). Modulation of human valve interstitial cell phenotype and function using a fibroblast growth factor 2 formulation. PLoS One 10, e0127844.

Li, J., Bowens, N., Cheng, L., Zhu, X., Chen, M., Hannenhalli, S., Cappola, T.P., and Parmacek, M.S. (2012). Myocardin-like protein 2 regulates TGFβ signaling in embryonic stem cells and the developing vasculature. Dev. Camb. Engl. 139, 3531–3542.

Li, Z., Gaudreault, N., Arsenault, B.J., Mathieu, P., Bossé, Y., and Thériault, S. (2020). Phenome-wide analyses establish a specific association between aortic valve PALMD expression and calcific aortic valve stenosis. Commun. Biol. 3, 1–8.

Lindman, B.R., Clavel, M.-A., Mathieu, P., Iung, B., Lancellotti, P., Otto, C.M., and Pibarot, P. (2016). Calcific aortic stenosis. Nat. Rev. Dis. Primer 2, 16006.

Luscombe, N.M., Laskowski, R.A., and Thornton, J.M. (2001). Amino acid-base interactions: a three-dimensional analysis of protein-DNA interactions at an atomic level. Nucleic Acids Res. 29, 2860–2874.

McLean, C.Y., Bristor, D., Hiller, M., Clarke, S.L., Schaar, B.T., Lowe, C.B., Wenger, A.M., and Bejerano, G. (2010). GREAT improves functional interpretation of cis-regulatory regions. Nat. Biotechnol. 28, 495–501.

Mumbach, M.R., Rubin, A.J., Flynn, R.A., Dai, C., Khavari, P.A., Greenleaf, W.J., and Chang, H.Y. (2016). HiChIP: efficient and sensitive analysis of protein-directed genome architecture. Nat. Methods 13, 919–922.

Nie, Y., Chen, H., Guo, C., Yuan, Z., Zhou, X., Zhang, Y., Zhang, X., Mo, D., and Chen, Y. (2017). Palmdelphin promotes myoblast differentiation and muscle regeneration. Sci. Rep. 7, 1–9.

de la Pompa, J.L., Timmerman, L.A., Takimoto, H., Yoshida, H., Elia, A.J., Samper, E., Potter, J., Wakeham, A., Marengere, L., Langille, B.L., et al. (1998). Role of the NF-ATc transcription factor in morphogenesis of cardiac valves and septum. Nature 392, 182–186.

Ranger, A.M., Grusby, M.J., Hodge, M.R., Gravallese, E.M., de la Brousse, F.C., Hoey, T., Mickanin, C., Baldwin, H.S., and Glimcher, L.H. (1998). The transcription factor NF-ATc is essential for cardiac valve formation. Nature 392, 186–190.

Rohs, R., West, S.M., Sosinsky, A., Liu, P., Mann, R.S., and Honig, B. (2009). The role of DNA shape in protein-DNA recognition. Nature 461, 1248–1253.

Rutkovskiy, A., Malashicheva, A., Sullivan, G., Bogdanova, M., Kostareva, A., Stensløkken, K.-O., Fiane, A., and Vaage, J. (2017). Valve interstitial cells: the key to understanding the pathophysiology of heart valve calcification. J. Am. Heart Assoc. 6, e006339.

Schlotter, F., Halu, A., Goto, S., Blaser, M.C., Body, S.C., Lee, L.H., Higashi, H., DeLaughter, D.M., Hutcheson, J.D., Vyas, P., et al. (2018). Spatiotemporal multi-omics mapping generates a molecular atlas of the aortic valve and reveals networks driving disease. Circulation 138, 377–393.

Siggers, T., and Gordân, R. (2014). Protein-DNA binding: complexities and multi-protein codes. Nucleic Acids Res. 42, 2099–2111.

Taylor, P.M., Allen, S.P., and Yacoub, M.H. (2000). Phenotypic and functional characterization of interstitial cells from human heart valves, pericardium and skin. J. Heart Valve Dis. 9, 150–158.

Thériault, S., Gaudreault, N., Lamontagne, M., Rosa, M., Boulanger, M.-C., Messika-Zeitoun, D., Clavel, M.-A., Capoulade, R., Dagenais, F., Pibarot, P., et al. (2018). A transcriptome-wide association study identifies PALMD as a susceptibility gene for calcific aortic valve stenosis. Nat. Commun. 9, 988.

Wang, J., Dayem Ullah, A.Z., and Chelala, C. (2018). IW-Scoring: an Integrative Weighted Scoring framework for annotating and prioritizing genetic variations in the noncoding genome. Nucleic Acids Res. 46, e47.

Welter, D., MacArthur, J., Morales, J., Burdett, T., Hall, P., Junkins, H., Klemm, A., Flicek, P., Manolio, T., Hindorff, L., et al. (2014). The NHGRI GWAS Catalog, a curated resource of SNP-trait associations. Nucleic Acids Res. 42, D1001–D1006.

Wild, P.S., Felix, J.F., Schillert, A., Teumer, A., Chen, M.-H., Leening, M.J.G., Völker, U., Großmann, V., Brody, J.A., Irvin, M.R., et al. (2017). Large-scale genome-wide analysis identifies genetic variants associated with cardiac structure and function. J. Clin. Invest. 127, 1798–1812.

Yang, L., Orenstein, Y., Jolma, A., Yin, Y., Taipale, J., Shamir, R., and Rohs, R. (2017). Transcription factor family-specific DNA shape readout revealed by quantitative specificity models. Mol. Syst. Biol. 13, 910.

Supplemental information

Enhancer-associated aortic valve stenosis risk

locus 1p21.2 alters NFATC2 binding site

and promotes fibrogenesis

Arnaud Chignon, Mickael Rosa, Marie-Chloé Boulanger, Déborah Argaud, Romain Devillers, Valentin Bon-Baret, Ghada Mkannez, Zhonglin Li, Anne Rufiange, Nathalie Gaudreault, David Gosselin, Sébastien Thériault, Yohan Bossé, and Patrick Mathieu

a

Normalized interactions

7.5
5.0
2.5
0.0

5.26   5.28   5.30
Position on chr11 (Mb)

HBB   HBD   HBBP1 BGLT3 HBG1 HBG2   HBE1

H3K27ac HiChIP 1D

LCR

b

NspI

HBB   HBD   HBBP1 BGLT3 HBG1 HBG2   HBE1   F1

LCR
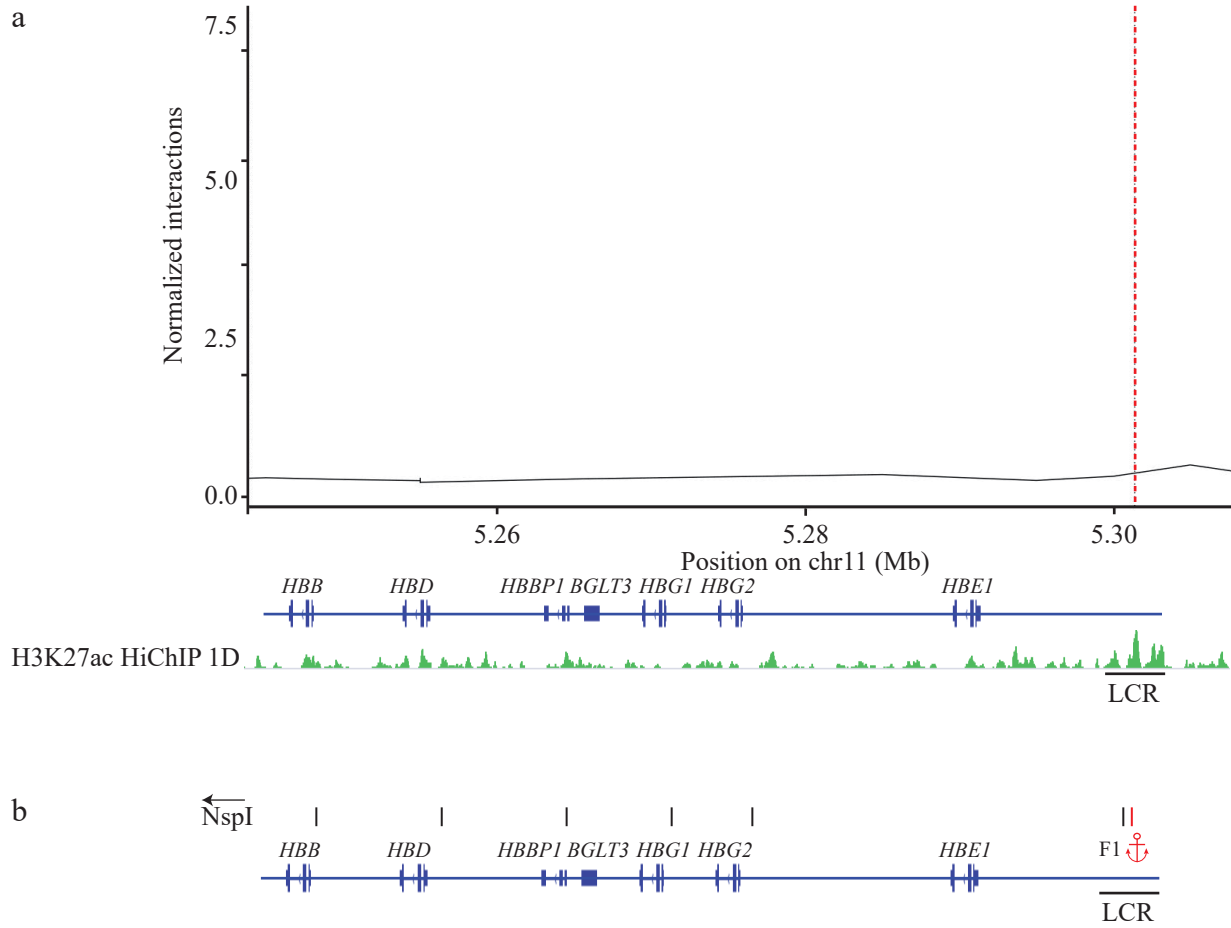
Figure S1, related to Figure 2: 3D chromatin profile at the beta globin locus in VICs. a) Virtual 4C analysis shows no contact at the beta globin locus in VICs, below H3K27ac HiChIP 1D track. b) NspI digestion pattern and chromosome conformation capture (3C) design at the beta globin locus. LCR: locus control region.
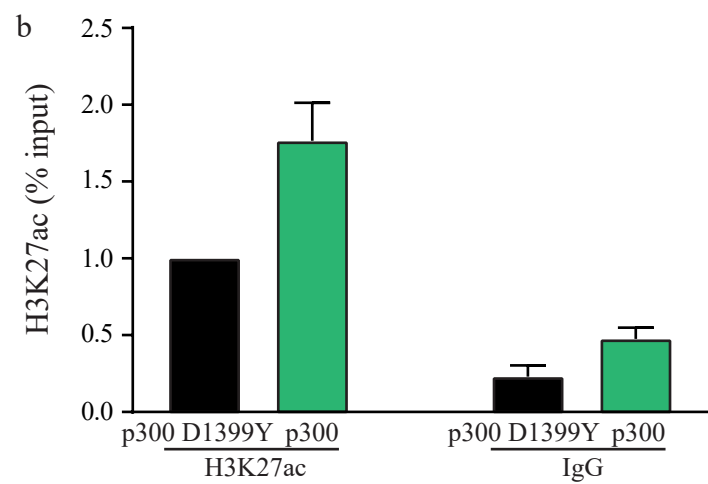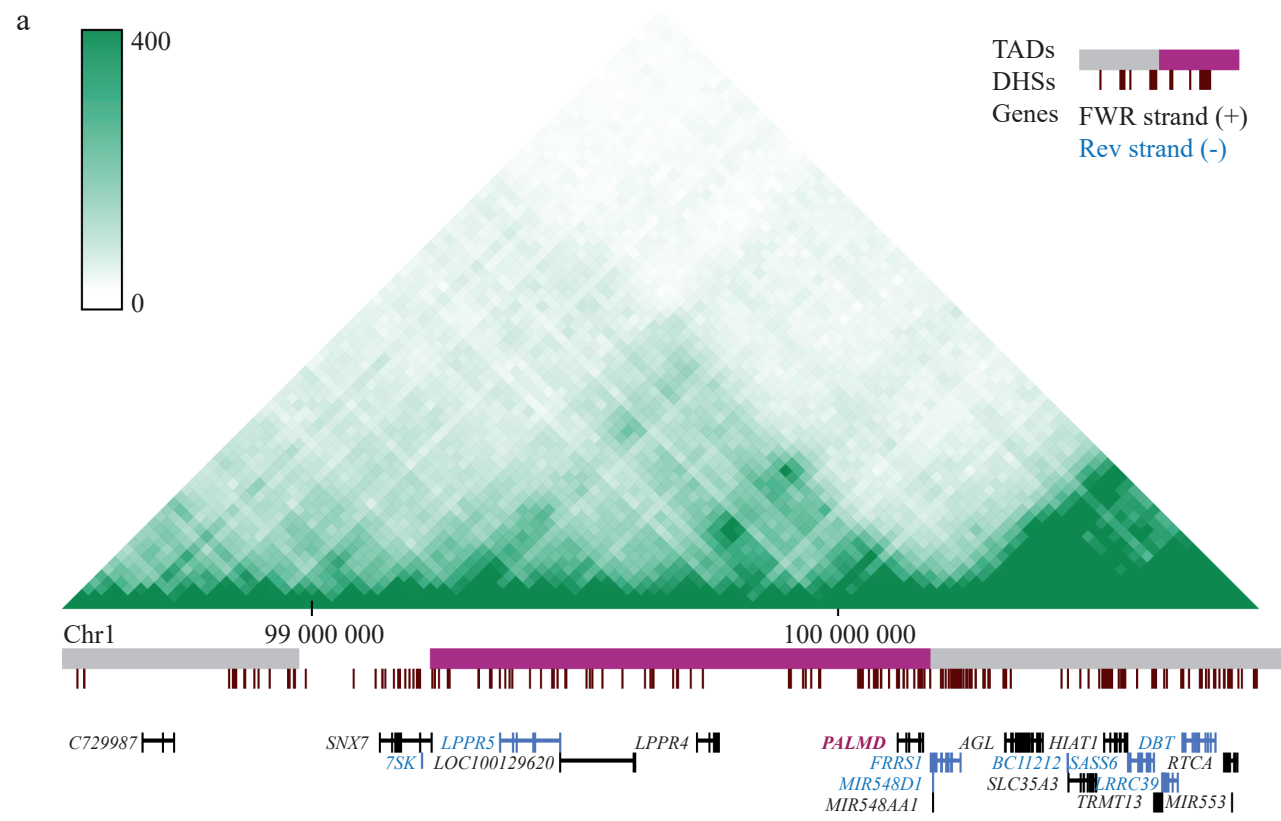
Figure S2, related to Figure 3: topologically associated domains (TADs) centered on rs6702619 and CRISPR activation acetylation at rs6702619. a) HiC data in mesenchymal cells; TADs are shown as horizontal grey and magenta (includes PALMD) horizontal bars. b) Chromatin immunoprecipitation with H3K27ac to verify increase in acetylation after CRISPR dCas9 targeting of p300 or mutant D1399Y (n=3).
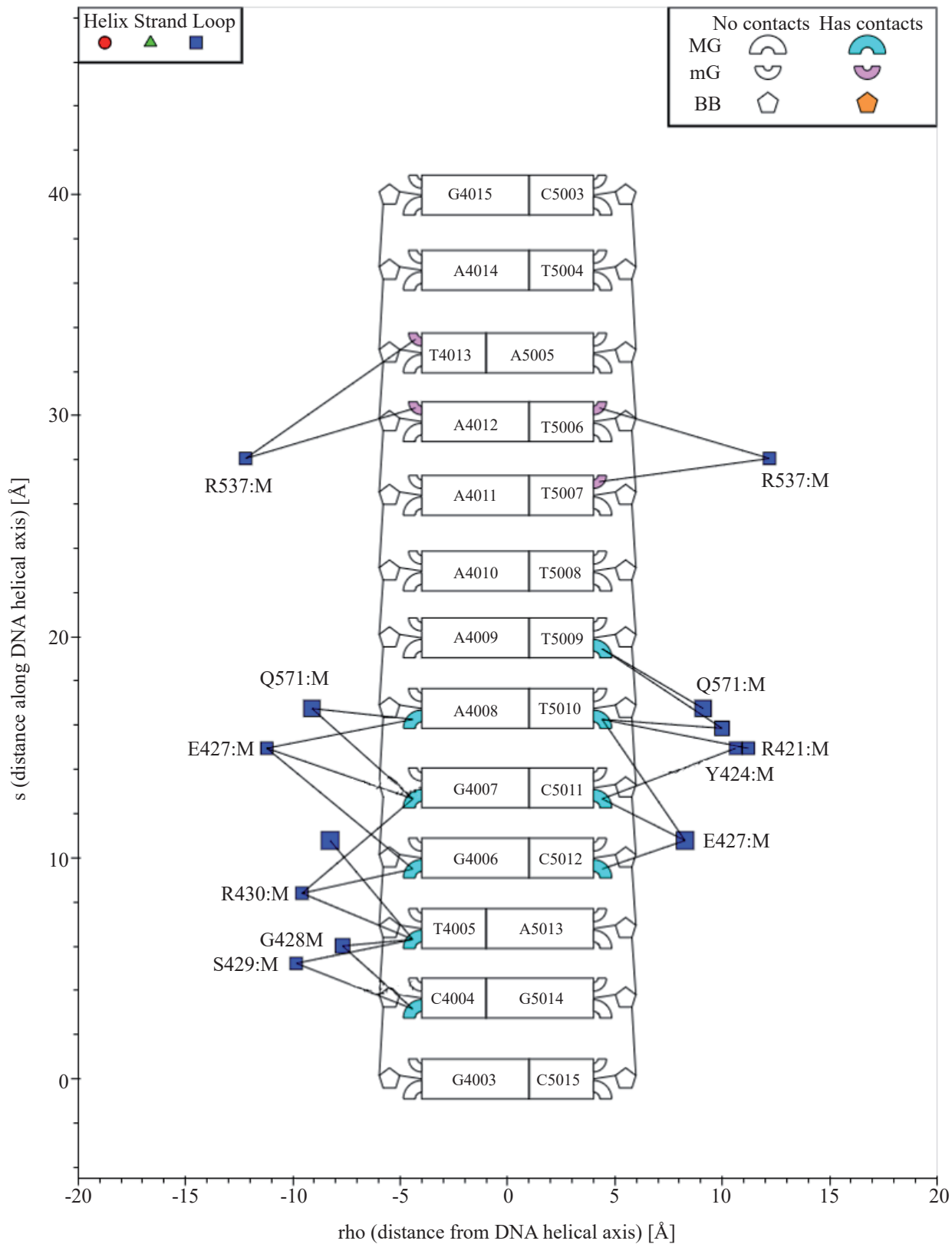
Figure S3, related to Figure 3: Contact map of NFATC2 with DNA. Linear contact map of NFATC2 interaction with the rs6702619 DNA
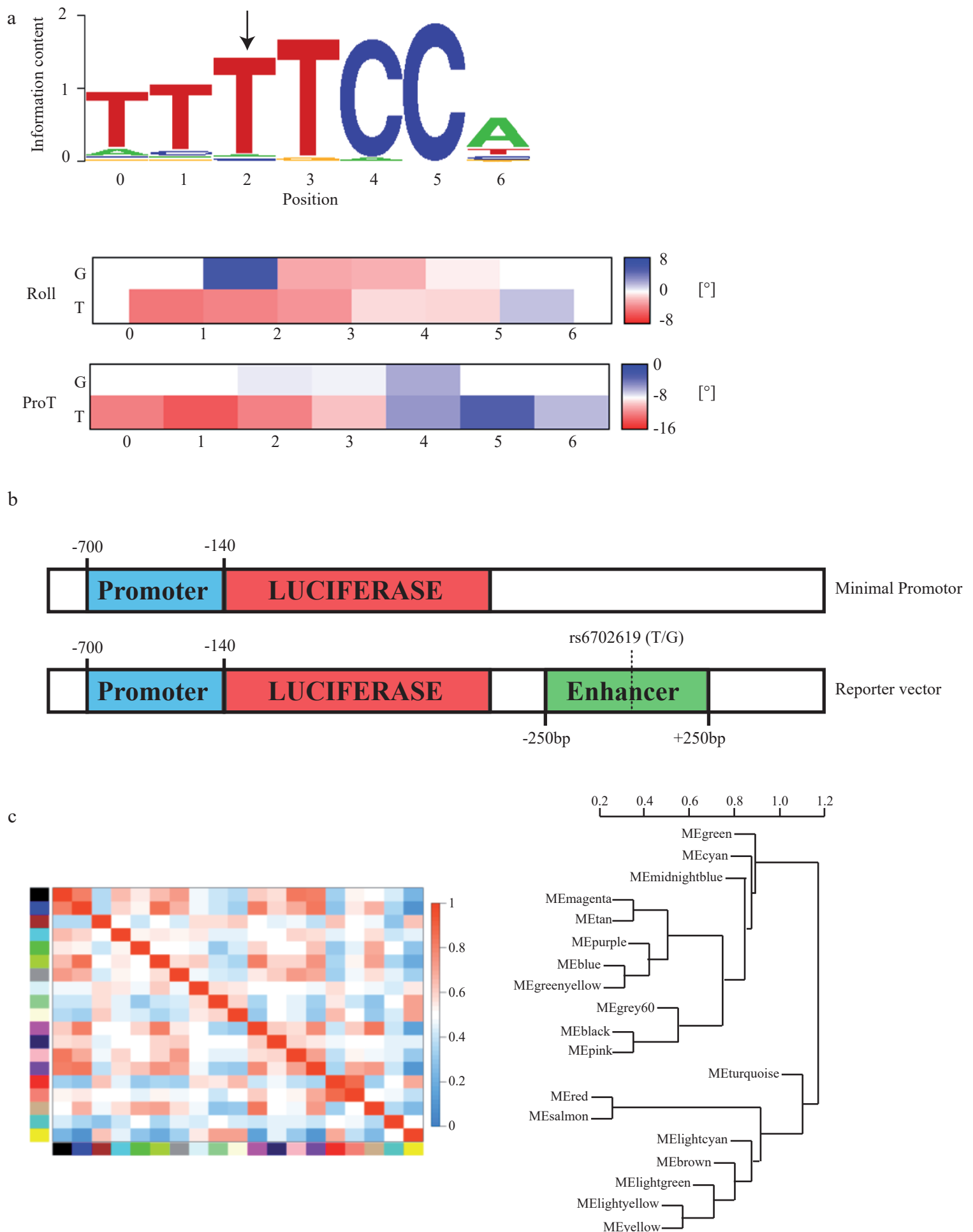
Figure S4, related to Figures 3 and 4: Position weighted matrix of NFATC2 binding site sequence, luciferase assay design and clustering of co-expression profile. a) Position weighted matrix of NFATC2 binding sequence and the effects of the T to G transition on roll and propeller twist of the double helix. b) Reporter assay constructions c) Clustering dendrogram of co-expression profile. The red module includes 283 genes and encompasses *PALMD*.
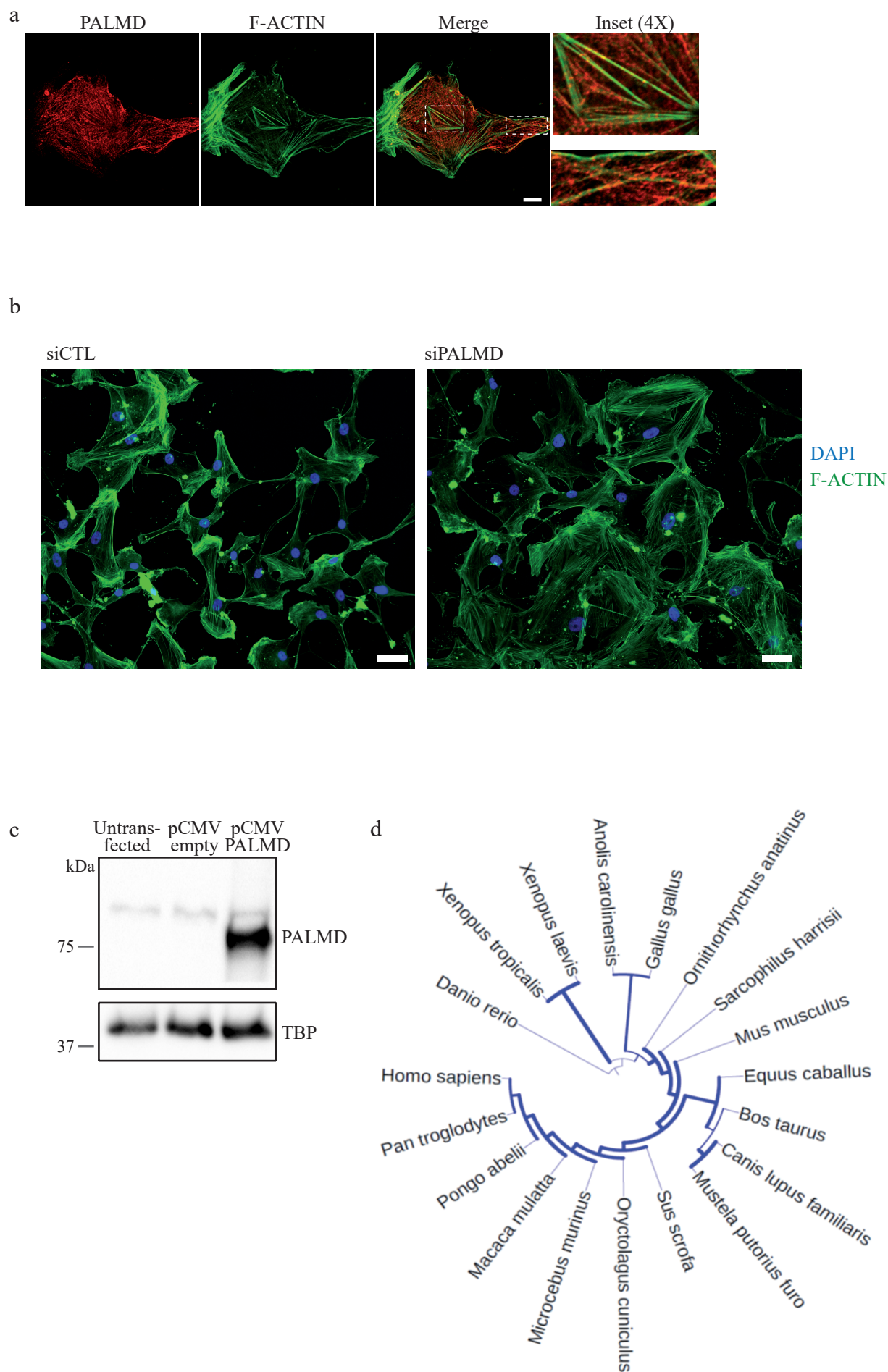
Figure S5, related to Figures 5 and 6: PALMD and F-actin co-distribution, effect of PALMD on the shape of VICs and conservation of the PALMD sequence. a) Confocal images showing PALMD and F-actin co-distribution, scale bar 10μm. b) Morphology of siCTL and siPALMD treated VICs, scale bar 50μm c) Western blot for PALMD in COS-7 cells (n=1). d) Analysis of amino acid sequence in different vertebrate species indicate that PALMD is highly conserved especially among the mammalian clades.

Supplemental Table 2, related to Figure 2:
Primer efficiencies for the 3C experiment at the 1p21.2 locus.

Primer sets with Tm (˚C)		Amplicon size (bp)	Efficiency
	Fragment 1 (59.50)	188	0.88
	Fragment 2 (60.25)	166	1.12
	Fragment 3 (59.53)	156	0.88
	Fragment 4 (57.53)	199	1.02
	Fragment 5 (59.33)	196	0.97
Anchor (59.03)	Fragment 6 (60.48)	199	1.21
	Fragment 7 (58.54)	162	1
	Fragment 8 (59.82)	209	1.26
	Fragment 9 (58.51)	206	1.05
	Fragment 10 (59.79)	152	0.84
	Fragment 11 (59.34)	207	1.18

Supplemental Table 3, related to Figure 2:

Ct obtained by qPCR after digestion and random ligation of a BAC spanning the 1p21.2 locus.

ND: not detectable.

Fragment	Ct
1	31.38
2	39.91
3	34.43
4	ND
5	ND
6	28.6
7	38.61
8	39.34
9	29.97
10	ND
11	36.69

Supplemental Table 4, related to Supplemental Figure 1:
Ct obtained by a 3C experiment at the beta globin locus in VICs.

ND: not detectable.

Gene	Ct
F1	31,38
HBG2	34,43
HBG1	38,61
HBBP1	36,69
HBD	39,91
HBB	ND

Supplemental Table 5, related to Figure 1: Conservation of the locus 1p21.2.

rsid	LD (r2)	chr	pos	PhastCons	PhyloP
rs6702619	1	1	100046246	1	3.39
rs6693824	0.64	1	100053597	0.204	0.37
rs954906	0.63	1	100053981	0.163	0.31
rs1339860	0.64	1	100054799	0	0.23
rs1856616	0.64	1	100051980	0.049	0.21
rs7543130	1	1	100049785	0	-0.04
rs1890753	0.96	1	100039519	0	-0.05
rs7543039	1	1	100049648	0	-0.80
rs11166276	1	1	100045239	0	-1.62

Supplemental Table 13: Primer sequences, related to figures 2, 3 and 6.

3C primers at the _PALMD_ locus

Fragment	Sequence (5'-3')
Anchor	AAGCAGGACTGAGAGAATGGA
1	TTGGGTGCAGAGAGAGATGA
2	ACTCAACTTCGCCTCCCTTT
3	GAGCAGATGCACAGATCAGG
4	ACCTAGTTTTCTCTTGTTTAATGCTT
5	TTCCCGGAACAAACATAAAAA
6	ATTTGCGTTTGGAACCTTCA
7	TGAGGTAGAGTGCCCAGAGA
8	CCTTTATGGGTGGGCTGTTA
9	CTCAGTCCCTGGGATTTTATG
10	TTCATATAAAATTGGGATTATTTTTGC
11	CCACATTCTCCACCAAATCA
GAPDH for	ACAGTCCATGCCATCACTGCC
GAPDH rev	GCCTGCTTCACCACCTTCTTG

3C primers at the beta globin locus

Fragment	Sequence (5'-3')
Anchor	CACCAAGACTGGCCTGAGAT
F1	AACCCTCACAGCTGCTAACC
HBE1	CTCAGCTCACTGCAACCTTC
HBG2	TGCTCGGTAAAGATGATGGT
HBG1	CCCATCATAGAGGATACCAGGA
HBBP1	CTCACCTCCAGCCTTCTCAC
HBD	ATCCACAAATGCTGGATGCT
HBB	AAAACCTTCTGGTAAGAAAAGAAAAA

qPCR primers

	Forward (5'-3')	Reverse (5'-3')
PALMD	GTGGAAAGAGAAGAAAGAG	CTGATGGCAGAGGTATT
FRRS1	GAAGTCACCCTGTAATGGACTC	CCAGGAAGGGTAATGTTTCTTCT
LPPR4	GAGCTGTCAGATTCGTTGGT	AGTAAGGTGCTTGATATCCTGTG
LPPR5	GAAGCAGCTCTCAGTGTCTATG	TTAGCAAGTCTGGTTCCCTTG
TGFB2	TGTAGCCCCATAACTTGGAT	GAGGAAATAGGGTGGGTTTT
MMP2	GCAGTTTGCTTTGTATGCAC	TGGAGAAGAGACTCGGTAGG
MMP9	CCAGTTTCCATTCATCTTCC	CGAGTACTCCTTACCCAGGA

ChIP primers

	Forward (5'-3')	Reverse (5'-3')
enhancer	GCCAGCCTCCACACATTAT	CTGCTTTGTCCCTGCCTATT

Transparent Methods

VICs isolation

Human VICs were isolated from control non-mineralized aortic valves obtained from patients undergoing heart transplantation. All donated tissues have been obtained with an explicit written consent approved by the local ethical committee and the investigations conducted in accordance with the Helsinki Declaration. Aortic leaflets were cut into pieces and incubated in 0.3% type I collagenase (Invitrogen, Thermo Fisher Scientific, ON, Canada) at 37°C for 45 minutes, then filtered through a 70 µm mesh, centrifuged for 5 minutes at 1,500 rpm and resuspended in complete media (DMEM, 10% FBS with L-glutamine and sodium pyruvate). Cells were used between passages 3 to 7.

ChIP-Seq Library Preparation and Sequencing

VICs were fixed with 1% formaldehyde at room temperature for 10 minutes and quenched with glycine to 0.125 M. Cells were harvested in 1 mL of PBS 1X/5% BSA (Sigma-Aldrich, ON, Canada), centrifuged 5 minutes at 800 x g at 4 °C and the supernatants were removed. Pellets were resuspended in 1 mL of lysis buffer L1A/B (10 mM Hepes-KOH pH 7.5, 85 mM KCl, 1 mM EDTA, 0.5% NP-40 containing PIC, PMSF and sodium butyrate) and incubated for 10 minutes on ice. Whole cellular extracts were centrifuged for 5 minutes at 8,000 x g and nuclei were sonicated on ice with a Bioruptor Standard Sonicator (Diagenode, NJ, USA) in 450 µL of L3 buffer (5 mM TrisHCl pH 7.5, 100 mM NaCl, 10 mM EDTA, 0.5 mM EGTA, 0.1% deoxycholate, 0.5% sarkosyl, supplemented with PIC, PMSF and sodium butyrate) for 3 minutes cycles alternating 10 seconds ON and 10 seconds OFF with 30% amplitude. Triton-X100 to final concentration of 1% was added and lysates

centrifugated for 5 minutes at 18,000 x *g* at 4°C. Nuclear extracts were then immunoprecipitated for 2 hours at 4°C with 2 µg of H3K4me3 (#9751, Cell Signaling Technology, New England Biolabs, ON, Canada), 2 µg of H3K4me1 (#5326, Cell Signaling Technology, New England Biolabs, ON, Canada) or 2 µg of H3K27Ac (#ab4729, Abcam, ON, Canada) pre-bound to protein G Dynabeads (Life Technologies, Thermo Fisher Scientific, ON, Canada). Samples were washed three times with ice cold wash buffer I (20 mM TrisHCl pH 7.5, 150 mM NaCl, 2 mM EDTA, 1% Triton X-100, 0.1% SDS, 2 mM EDTA), wash buffer II (10 mM TrisHCl, 250 mM LiCl, 1% NP-40, 0.7% deoxycholate, 1 mM EDTA) and TET (10 mM TrisHCl pH 7.5, 1 mM EDTA, 0.1% Tween-20). DNA-proteins complex were eluted with 100 µL of 1% SDS/TE at room temperature for 40 minutes. After addition of NaCl to 300 mM final concentration, crosslink was reversed at 65°C overnight. Samples were digested with 0.33 mg/mL of RNase A (Qiagen, ON, Canada) for 1 hour at 37°C and proteins digested for 1 hour at 55°C with 0.5 mg/mL of proteinase K (Qiagen, ON, Canada). DNA was purified using DNA clean up & concentrator kit (Zymo Research, Cedarlane, Canada). Libraries for ChIP-seq were constructed using the QIAseq Ultralow Input Library Kit (Qiagen, ON, Canada). Libraries were PCR-amplified for 10-12 cycles. Fragments of 200-1,000 bp were selected according to manufacturer's instructions. As a control, 1% input chromatin libraries after sonication were sequenced for each ChIP samples. Sequencing was performed using 75-bp reads on an Illumina HiSeq4000 (UCSD IGM Genomics Facility, CA, USA).

ATAC-seq

Nuclei from approximatively 2.5-4 x 10^5 cells were prepared and treated as previously described(Shashikant et al., 2018) with a few modifications. Transposition reactions were

performed using the Tn5 Transposase and TD reaction buffer from the Nextera DNA library preparation kit (Illumina, CA, USA) for 30 minutes at 37°C. Immediately following transposition, the transposed DNA were purified using DNA clean up & concentrator kit (Zymo Research, Cedarlane, Canada). DNA were eluated in 20 μL of elution buffer (Buffer EB from DNA clean up & concentrator kit). Libraries were first amplified for 5 cycles using custom-synthesized index primers and then a second amplification was performed. The appropriate number of additional PCR cycles was determined using quantitative real-time PCR by plotting the Rn value (fluorescent signal from SYBR Green I) versus cycle number and determining the cycle number corresponding to one-third of the maximum fluorescent intensity. Libraries were PCR-amplified for 4-7 cycles. After PCR amplification, libraries were purified using DNA clean up & concentrator kit (Zymo Research, Cedarlane, Canada). Library quality was assessed on a BioAnalyser (Agilent, ON, Canada) using Agilent High Sensitivity DNA kit (Agilent, ON, Canada). Sequencing was performed using 75-bp reads on an Illumina HiSeq4000 (UCSD IGM Genomics Facility, CA, USA).

ChIP-Seq and ATAC-seq data analysis

FASTQ files from sequencing experiments were mapped to the UCSC genome build hg19 using Bowtie2 with default parameters. BigWIG were generated by using bamcoverage tool and peaks were called using MACS2. GREAT(McLean et al., 2010) was used to determine Gene Ontology (GO) terms associated with H3K4me1 peaks in VICs.

HiChIP

H3K27ac HiChIP was performed as described previously(Mumbach et al., 2016). About 1 million of VICs were crosslinked with 1% formaldehyde for 15 minutes and quenched by glycine (0.125 M final). Cells were resuspended with 500 µL of cold HiC lysis buffer (10 mM TrisHCl pH 8.0, 10 mM NaCl, 0.2% NP-40, supplemented with PIC, Sigma-Aldrich, ON, Canada) with rotation at 4°C for 30 minutes. Nuclei were isolated by centrifugation at 2,500 x g for 5 minutes at 4°C, washed with cold HiC lysis buffer, resuspended with 0.5% SDS and incubated for 10 minutes at 62°C. 285 µL of water and 50 µL of 10% Triton X-100 were then added to quench SDS followed by an incubation at 37°C for 15 minutes. Chromatin was digested 2 h at 37°C by addition of 40 U of MboI restriction enzyme and 50 µL of CutSmart buffer 10X (New England BioLabs, ON, Canada). Enzyme was inactivated at 62°C for 20 minutes. To mark DNA overhangs with biotin, a mix containing biotin–dATP, dCTP, dGTP, dTTP (Thermo Fisher, ON, Canada) and DNA Polymerase I Klenow fragment (New England BioLabs, ON, Canada) was added, followed by an incubation at 37°C for 1 hour with rotation. Ligation was then performed at room temperature for 4 hours with rotation by addition of a ligation master mix containing ligase buffer (New England BioLabs, ON, Canada), 10% Triton X-100, BSA (Thermo Fisher, ON, Canada), 4,000 U of T4 ligase (New England BioLabs, ON, Canada), and 660 µL of water. Nuclei were then isolated by centrifugation at 2,500 x g for 5 minutes and resuspended in Nuclear lysis buffer (50 mM Tris-HCl pH 7.5, 10 mM EDTA, 1% SDS, supplemented with PIC, Sigma-Aldrich, ON, Canada) before sonication on ice with a Bioruptor Standard Sonicator (Diagenode, NJ, USA). Sample was clarify for 15 minutes at 16,100 x g at 4°C and 800 µL of ChIP Dilution buffer (0.01% SDS, 1.1% Triton X-100, 1.2 mM EDTA, 16.7 mM Tris-HCl pH 7.5, 167 mM NaCl) were added. 34 µL of protein

G Dynabeads (Life Technologies, Thermo Fisher Scientific, ON, Canada) were washed and resuspended in 50 µL of ChIP Dilution buffer. Sample was then added to beads, followed by an incubation at 4ºC for 1 hour with rotation. Sample was put on a magnet and supernatant removed into a new tube. 4 µg of H3K27ac antibody (#ab4729, Abcam, ON, Canada) were added, and the sample was incubated overnight at 4ºC with rotation. 34 µL of protein G Dynabeads in 50 µL of ChIP dilution buffer were added to the sample for an incubation at 4ºC for 2 hours. Beads were then washed sequentially with Low Salt Wash buffer (0.1% SDS, 1% Triton X-100, 2 mM EDTA, 20 mM TrisHCl pH 7.5, 150 mM NaCl), High Salt Wash buffer (0.1% SDS, 1% Triton X-100, 2 mM EDTA, 20 mM Tris-HCl pH 7.5, 500 mM NaCl) and LiCl wash buffer (10 mM Tris-HCl pH 7.5, 250 mM LiCl, 1% NP-40, 1% sodium deoxycholate, 1 mM EDTA), and resuspended in 100 µL of DNA Elution buffer (50 mM sodium bicarbonate pH 8.0, 1% SDS). Sample was incubated at room temperature for 10 minutes with rotation followed by 3 minutes at 37ºC shaking, and then placed on a magnet. The supernatant was then transferred in a new tube and another 100 µL of DNA Elution buffer was added to the beads for another same incubation to obtain 200 µL of sample. Reverse-crosslink was performed by addition of Proteinase K (Qiagen, ON, Canada) and a first incubation at 55ºC for 45 minutes with shaking followed by a second incubation at 67ºC for 1.5 hours. DNA was then purified with clean up & concentrator kit (Zymo Research, Cedarlane, Canada) and quantified with QuBit (Thermo Fisher, ON, Canada). 5 µL of Streptavidin C-1 beads (Life Technologies, Thermo Fisher Scientific, ON, Canada) were washed with Tween Wash buffer (5 mM Tris-HCl pH 7.5, 0.5 mM EDTA, 1 M NaCl, 0.05% Tween-20) and resuspended in 10 µL of 2X Biotin Binding buffer (10 mM Tris-HCl pH 7.5, 1 mM EDTA, 2 M NaCl). Sample was then added

for an incubation of 15 minutes at room temperature with rotation, and placed on a magnet. Supernatant was discarded and beads washed twice by adding 500 µL of Tween Wash buffer and incubating at 55ºC for 2 minutes shaking. Beads were washed in 100 µL of 1X TD buffer (2X TD buffer is 20 mM Tris-HCl pH 7.5, 10 mM magnesium chloride, 20% dimethylformamide), and then resuspended in 25 µL of 2X TD buffer, an appropriate amount of Tn5 adjusted for the DNA quantity (about 5 ng) and water to 50 µL, followed by an incubation at 55ºC for 10 minutes with interval shaking. Sample was then placed on a magnet and supernatant removed. 100 µL of 50 mM EDTA were then added to the sample for an incubation at 50ºC for 30 minutes, followed by two washes at 50ºC for 3 minutes, and two additional washes in Tween Wash buffer at 55ºC for 2 minutes. Beads were then resuspended in 10 mM Tris. Sample was placed on magnet and beads resuspended in 50 µL of a PCR master mix (25 µL of Phusion HF 2X (New England BioLabs, ON, Canada), 1 µL of each Nextera Ad1_noMX and Nextera Ad2.1 at 12.5 µM, and 23 µL of water). The following PCR program was performed: 72 °C for 5 min, 98 °C for 1 min, then cycle at 98 °C for 15 s, 63 °C for 30 s, and 72 °C for 1 min. Cycle number was set to 10 considering the amount of DNA. Library was placed on a magnet and eluted into a new tube before purification with clean up & concentrator kit (Zymo Research, Cedarlane, Canada). Library size selection (300-700 bp) was performed by cutting a 2% agarose gel and DNA purified with PureLink Quick Gel Extraction (Thermo Fisher, ON, Canada). Library quality was assessed on a BioAnalyser (Agilent, ON, Canada) using Agilent High Sensitivity DNA kit (Agilent, ON, Canada). Paired-end sequencing with 690 million reads was performed with NovaSeq 6000 S4 (UCSD IGM Genomics Facility, CA, USA).

HiChIP data processing

Paired-end reads were aligned using HiC-Pro(Servant et al., 2015) with default settings. Contact matrix was generated with Juicer from the allValidPairs file generated by HiC-Pro. Most confident interactions ($P_{FDR} < 1$ x 10^{-6}) were determined with HOMER with the BAM.homer file converted by the hicup2homer tool available from HiCUP. The matrix normalized by the vanilla coverage square root for the chromosome 1 at a 5 kb resolution was dumped using Juicer. This matrix was used to generate the virtual 4C with R considering the interactions with a bin containing the rs6702619. H3K27ac HiChIP 1D track was generated using bamcoverage from the BAM file generated by HiC-Pro.

Chromosome conformation capture (3C)

3C experiments were performed as described previously(Hagège et al., 2007). Briefly, 10 millions of VICs were crosslinked with 1% formaldehyde for 15 minutes, quenched by glycine (0.125 M final), and lysed with cold lysis buffer (10 mM TrisHCl pH 7.5, 10 mM NaCl, 0.2% NP-40, supplemented with PIC, Sigma-Aldrich, ON, Canada). Nuclei were isolated by centrifugation at 400 x *g* for 5 minutes at 4°C, and then resuspended in CutSmart buffer 1.2X (New England BioLabs, ON, Canada) plus 0.3% SDS. Nuclei were incubated 1hour at 37°C while shaking at 900 rpm before the addition of Triton X-100 (2% final) and incubated another hour with the same conditions. DNA were digested overnight at 37°C with 400 U of NspI (New England BioLabs, ON, Canada), and the enzyme was then inactivated by addition of 1.6% SDS at 65°C for 25 minutes. Reactions were then diluted for 20-fold by ligation buffer 1.15X (New England BioLabs, ON, Canada) with 1% Triton X-100, and ligated with 1,000 U of T4 ligase (New England BioLabs, ON, Canada) at 16°C overnight. Reverse crosslink was then performed by Proteinase K (Qiagen, ON, Canada) addition at 65°C overnight. RNA was digested with RNase A (Qiagen, ON,

Canada) and ligated DNA fragments were then purified by phenol/chloroform extraction, and analyzed by quantitative real-time PCR (qPCR).

Quantification of ligated products was performed by qPCR using the NspI cutting site located upstream the rs6702619 as the anchor. For all fragments, we first normalized using a genomic *GAPDH* undigested control, then we used the level of ligation products between the anchor and the nearest downstream NspI site (#1) as a strong normalizer to correct for genomic random interactions as described previously(Dekker, 2006; Hagège et al., 2007). Bacterial artificial chromosome (BAC) (RP11-612E8) from BACPAC Resources Center (https://bacpacresources.org/) spanning the genomic region containing the rs6702619 and *PALMD* (GRCh37/hg19 chr1: 99966146-100154958) was used to assess the primer efficiencies and as a negative random ligation control (**Supp. Table 2 and 3**). Primer efficiencies were calculated for each primer set with the formula $E=10^{(-1/slope)}$. An additional 3C experiment at the beta globin locus in VICs was performed as a supplemental negative control (**Supp. Table 4**). Two biological replicates were conducted and qPCR were performed in triplicates to improve sensitivity. Primers sequences are provided in the Supplemental Table 13.

Cell transfection

HEK-293T cells were transfected by using the calcium phosphate technique. For knockdown experiments, VICs were transfected with HiPerFect transfection reagent (Qiagen, ON, Canada) and for overexpression experiments VICs and COS-7 were transfected with Nanojuice transfection reagent (EMD Millipore, VWR, QC, Canada). Following 72 hours transfection of siRNAs; siCTL (All Star negative control siRNA#1027281), siPALMD (siPALMD#2:SI04247502), siNFATC2

(siNFATC2#7:SI00099519) (Qiagen, ON, Canada), or 48 hours of dCas9-p300 constructs;

pcDNA-dCas9-p300 (Addgene#61357), pcDNA-dCas9-p300D1399Y, (Addgen#61358)

(MA, USA) cells were harvested in RTK lysis buffer from E-Z Nucleic Acid (E.Z.N.A.®)

kit (Omega Bio-tek, VWR, QC, Canada).

Chromatin immuno-precipitation (ChIP)

Cells were homogenized in 1 mL of PBS 1X containing PIC (Sigma-Aldrich, ON, Canada).

The homogenized samples were centrifuged 5 minutes at 800 x g at 4°C. The supernatants

were removed and pellets were resuspended in PBS 1X containing PIC (Sigma-Aldrich,

ON, Canada) and centrifuged 5 minutes at 800 x g at 4°C. Pellets were then resuspended

in 500 µL of lysis buffer (50 mM Hepes-KOH pH 7.5, 140 mM NaCl, 1 mM EDTA, 1%

Triton X-100, 0.1% sodium deoxycholate, 0.1% SDS, supplemented with PIC, Sigma-

Aldrich, ON, Canada). Sonication led to fragmentation of an average length of 400 bp. 2

µg of antibodies against H3K27ac (Active Motif, Cedarlane, ON, Canada) or isotype IgG

(Cell Signaling Technology, New England Biolabs, ON, Canada) were incubated with

proteins G dynabeads (Life technologies, Thermo Fisher Scientific, ON, Canada) for 6

hours before DNA samples were added to the antibodies/dynabeads mixtures and incubated

at 4°C overnight on a rotator. The next day, samples were washed with low salt buffer

(0.1% SDS, 1% Triton X-100, 2 mM EDTA, 20 mM TrisHCl pH 8.0, and 150 mM NaCl).

A second washing with high salt buffer (0.1% SDS, 1% triton X100, 2 mM EDTA, 20 mM

TrisHCl pH 8, and 500 mM NaCl) was performed, followed with LiCl buffer (10 mM

TrisHCl pH 8, 250 mM LiCl, 1 mM EDTA, 1% NP-40) and finally with TE buffer (10 mM

Tris-HCl, pH 8, 1 mM EDTA). The complex was then eluted by adding 200 µL of elution

buffer (1% SDS, 100 mM NaHCO$_3$) at 65°C for 1 hour. Eluted samples were reverse

crosslinked at 65°C overnight. DNA fragments were purified using DNA clean up & concentrator kit (Zymo Research, Cedarlane, Canada) and samples were analysed by qPCR assay using primers specific to the enhancer region (see the Supplemental Table 13 for primers sequences).

Real-time polymerase chain reaction

Total RNA was isolated with RNeasy micro kit from E-Z Nucleic Acid (E.Z.N.A.®) kit following manufacturer's instructions (Omega Bio-tek, VWR, QC, Canada). One μg of RNA was reverse transcribed using the Qscript cDNA supermix from Quanta (VWR, QC, Canada). qPCR were performed with perfecta sybr supermix from Quanta on the Rotor-Gene 6000 system (Corbett Robotics Inc, CA, USA). Primers for *PALMD*, *FRRS1*, *LPPR4*, *LPPR5*, *TGFB2*, *MMP2* and *MMP9* were obtained from IDT (IDT, IL, USA) (see the Supplemental Table 13 for sequences). Primers for *ACTA2*, *COL1A1* and *COL1A2* were purchased from Qiagen (ON, Canada). The expression of the hypoxanthine-guanine phosphoribosyltransferase (*HPRT*) (Qiagen, ON, Canada) was used as a reference to normalize the results.

NFATC2-DNA interaction

NFATC2 binding site at 1p21.2 risk locus was predicted by SNP2TFBS(Kumar et al., 2017) and TRANSFAC/JASPAR. Binding to DNA was illustrated with UCSF Chimera software (http://www.rbvi.ucsf.edu/chimera)(Pettersen et al., 2004) (PDB code : 1OWR). Nucleotide-residue contact map was generated with DNAproDB tool (http://dnaprodb.usc.edu/index.html)(Sagendorf et al., 2017).

DNA shape analysis

DNA shape modifications around rs6702619 were evaluated with tools provided by Rohs laboratory (https://rohslab.usc.edu/tools.html). Minor groove width, roll, propeller twist and helix twist were analyzed. DNA sequence 5'-TTGTCCA-3' containing rs6702619 was compared to the reference NFATC2 binding site sequence 5'-TTTTCCA-3' with TFBSshape tool (http://oldrohslab.usc.edu/TFBSshape/)(Yang et al., 2014).

Electrostatic potential analysis

Electrostatic potential of DNA sequence 5'-AACTATTTTTCCAGC-3' containing a NFATC2 binding site was analyzed with PBEQ Solver, a software solving the Poisson-Boltzmann equation allowing the characterization of the electrostatic potential on a macromolecular surface (http://www.charmm-gui.org/?doc=input/pbeqsolver)(Jo et al., 2008). Modification of electrostatic potential by rs6702619 was determined with DNAphi Rohs laboratory tool (https://rohslab.usc.edu/DNAphi/index.html) .

Luciferase reporter assay

VICs were transfected with the pGL4.10 luciferase vector (Promega, WI, USA) containing a minimal promoter with or without the enhancer region located around the rs6702619 (Gene synthesis and subcloning, Bio Basic, ON, Canada) along with the NFATC2 construction where indicated. COS-7 were transfected with a vector encoding Serum Factor (SRF) response elements (Promega, WI, USA) along with either an empty vector as control or a vector encoding for PALMD (GeneCopoeia, MD, USA). Both VICs and COS-7 cells were also transfected with a vector encoding for the renilla luciferase (Promega, WI, USA) as a reporter for transfection efficiency. At 48 hours post-transfection, cells were harvested

and luciferase activity was measured using the Dual-Luciferase Reporter Assay System, according to manufacturer's instructions (Promega, WI, USA).

DNA-protein ELISA

DPI-ELISA was performed as described before(Brand et al., 2010). Briefly, microtiter 96-well high binding plates (Greiner Bio-one, VWR, QC, Canada) were coated with streptavidin (500 pmol/well) (Sigma-Aldrich, ON, Canada) for 1 hour at room temperature. DNA probes (200 pmol/well) were incubated at 37°C for 1 hour. Plates were blocked for 30 minutes with PBS 1X/0.05% Tween-20/5% non-fat dry milk. Protein extracts were added and incubated for 1 hour. Rabbit anti-NFATC2 antibody (dilution:1/750) (Cell Signaling Technology, New England Biolabs, ON, Canada), 50 µL/well, was incubated with the plates for 60 minutes. HRP-labeled goat anti-rabbit antibody at 0.01 µg/mL (Millipore, Burlington, USA), 50 µL/well, was added for 1 hour. OPD (100 µL) (Thermo Fisher Scientific, ON, Canada) (0.5 mg/mL) was added for 30 minutes, then 100 µL of sulfuric acid (2.5 M) was added to stop the reaction. Absorbance was read on a spectrophotometer (λ=492 nm) (FilterMax F3 microplate reader, Molecular Devices, VWR, QC, Canada). Results are expressed in relative light absorbance units (RLU) after subtraction of the background. Excess material was washed off (with PBS 1X/0.05% Tween) between different steps.

Weighted Gene Co-Expression Network

Array-based whole-genome expression (Illumina HumanHT-12 v4 Expression BeadChip) from 233 human calcified aortic valve samples was obtained(Thériault et al., 2018). Clinical data of these patients were collected. Weighted gene co-expression network

analysis (WGCNA) was performed to assess connectivity and to provide biological significance of gene expression pattern. WGCNA was performed using the R package WGCNA(Langfelder and Horvath, 2008). Annotation of generated modules was performed using Metascape (http://metascape.org)(Tripathi et al., 2015).

Western blotting

Cell extracts were boiled for 10 minutes and proteins were loaded onto polyacrylamide gels followed by electrophoresis and transferred to nitrocellulose membranes. Membranes were blocked with TBS 1X/0.1% Tween-20 containing 5% non-fat dry milk (Sigma-Aldrich, ON, Canada), incubated with either PALMD (NBP1-88481, Novus Biologicals, Cedarlane, ON, Canada), α-ACTIN (#A2547, Sigma-Aldrich, ON, Canada), NFATC2 (#5861S), COL1A1 (#84336S) or GAPDH (#2118, Cell Signaling Technology, New England Biolabs, ON, Canada) antibodies overnight at 4°C. Membranes were then washed and incubated with HRP-labeled secondary antibodies (TransBionovo Co., Civic Biosciences Ltd, QC, Canada). Detection was done using clarity western ECL substrate (BioRad, ON, Canada). Images were acquired and quantification analyses were performed using a ChemiDocMP system and the Image Lab software (BioRad, ON, Canada).

Immunofluorescence of cells

Human VICs were seeded on poly-L-lysine coated glass coverslips. Cells were washed once with PBS 1X and fixed in 3.7% formaldehyde for 30 minutes at room temperature. Cells were treated 20 minutes with 50 mM NH$_4$Cl in PBS 1X and permeabilized for 10 minutes in PBS 1X containing 0.2% Triton X-100. Cells were then incubated in PBS 1X containing 5% milk for one hour at room temperature with constant agitation. Incubation

with anti-PALMD (#NBP1-88481, Novus Biologicals, Cedarlane, ON, Canada) or anti-VINCULIN (#V9131, Sigma-Aldrich, ON, Canada), was performed in PBS 1X containing 1% milk overnight at 4°C. Cells were washed four times with PBS 1X, followed with one hour incubation with FITC-conjugated anti-rabbit or anti-mouse secondary antibodies (Molecular Probes, Thermo Fisher Scientific, ON, Canada). F-actin was labeled, where indicated, by incubating cells for 1 hour with alexa488-labelled phalloidin (1/50) (Thermo Fisher Scientific, ON, Canada). Slides were mounted and analysed and confocal images were acquired using a Zeiss microscope LSM800 driven by the Zen software (Objective 63X oil, 1.4 NA, Zeiss, ON, Canada). Image processing and quantification were performed with ImageJ 1.47g (NIH, USA).

Triton extraction

Cells were extracted for 20 seconds in 0.1% Triton X-100 before fixation in 3.7% formaldehyde, then the immunofluorescence protocol was performed as usual, but omitting the permeabilization step.

Nuclear extracts preparation

Nuclear extracts were obtained by using NE-PER^{TM} Nuclear and cytoplasmic Extraction Reagent following the manufacturer's instructions (Thermo Fisher Scientific, ON, Canada).

PALMD interactome determination

HEK-293T cells were transfected with a vector expressing the human PALMD sequence HA tagged (GeneCopoeia, MD, USA). At 24 hours post-transfection, cell were harvested. Antibody against HA (Sigma-Aldrich, ON, Canada) was incubated with proteins G

dynabeads (Thermo Fisher Scientific, ON, Canada) for 10 minutes before cell lysates were added to the antibody/dynabeads mixture and incubated at 4°C overnight on a rotator. The next day, the samples were washed with PBS 1X/0.05% Tween-20. For PALMD interactome determination, beads were washed 4 times with ammonium bicarbonate and were dry frozen until LC-MS/MS was performed at the Quebec's CRCHU proteomic facility (QC, Canada). Data were analyzed with Scaffold Software and gene ontology (GO) terms enrichments were performed with Metascape.

Immunoprecipitations

VICs were rinsed once with ice-cold PBS 1X. Cells were next lysed, in a 1X cell lysis buffer (Cell Signaling Technology, New England Biolabs, ON, Canada) containing 1 mM PMSF and sonicated (3 times for 5 seconds at 30% intensity). Samples were centrifuged at 14,000 x g for 10 minutes at 4°C. A pre-clearing was performed with 20 μL of beads slurry on 200 μL of cell lysates (0.5 mg/mL of proteins) for 45 minutes, with rotation at 4°C. Primary antibodies were added to the lysates and incubated with rotation overnight at 4°C, afterward 25 μL of beads slurry was added to the lysates and samples were incubated with rotation during 25 minutes at 4°C. Immunoprecipitation complexes were washed 5 times with 1X cell lysis buffer, beads were resuspended in sample buffer, boiled and proteins were analyzed by western blot. Immunoprecipitations were performed using primary antibodies to α-SMA (#48938S, Cell Signaling Technologies, New England Biolabs, ON, Canada, 1 μL antibody /200 μL of lysates) and anti-PALMD (#16531-1-AP, Proteintech Group Inc, Cedarlane, ON, Canada, 1 μL antibody /200 μL of lysates). 10% input was used as positive control, mouse IgG (Cell Signaling Technology, New England Biolabs, ON, Canada) was used as negative control of the α-SMA IP, and rabbit IgG (Cell Signaling

Technology, New England Biolabs, ON, Canada) was used as negative control of the PALMD IP.

Proximity Ligation Assay

The proximity ligation assay (Olink Bioscience, Sigma-Aldrich, ON, Canada) was performed according to the manufacturer's instructions using monoclonal antibody against α-ACTIN (#A2547, Sigma-Aldrich, ON, Canada) and polyclonal antibody against PALMD (#NBP1-88481, Novus Biologicals, Cedarlane, ON, Canada).

Blot Overlay Assay

HEK-293T were transfected with a vector encoding PALMD-HA (GeneCopoeia, MD, USA) to produce PALMD rich extracts. Cells were extracted in cell lysis buffer (Cell Signaling Technology, New England Biolabs, ON, Canada) and sonicated (3 times for 5 seconds at 30% intensity), samples were centrifuged at 14,000 x g for 10 minutes at 4°C, supernatants were flash freezed and kept at -80°C until further used. Nitrocellulose membrane was pre-wetted in transfert buffer (Bio-Rad, CA, USA). F- and G-actin (2 and 5 µg, Cytoskeleton Inc., Cedarlane, ON, Canada) or actin dilution buffer (negative control, Cytoskeleton Inc., Cedarlane, ON, Canada) were blotted on membrane using Bio-Dot apparatus (Bio-Rad, CA, USA). The membrane was washed for 5 minutes in TBS 1X containing 0.1% Tween-20. The membrane was blocked for 1 hour in 5% BSA in TBS 1X and then it was incubated with PALMD-HA cell extracts (200 µg total proteins in TBS 1X) for 2 hours at room temperature with agitation. The membrane was washed 3 times for 5 minutes in TBS 1X-0.1% Tween-20 and blocked a second time in 5% milk in TBS 1X before western blotting(Wu et al., 2017).

Actin Polymerization Assay

PALMD effect on actin polymerization was assessed using an Actin Polymerization Biochem Kit (Cytoskeleton Inc., Cedarlane, ON, Canada) according to the manufacturer's instructions. Pyrene-G actin was prepared by adding 5 µL frozen aliquots of pyrene actin to 1.035 µL ice-cold G buffer (final concentration 2 µM). Actin oligomers were depolymerized by incubating on ice for 2 hours. After centrifugation at 14,000 x *g* for 30 minutes at 4°C, the supernatant consisting in the G-actin stock was transferred to a new tube. G-actin stock (100 µL) was incubated with 1 µM or 2 µM of recombinant PALMD (OriGene, Cedarlane, ON, Canada) 30 minutes at room temperature. Actin polymerization was initiated by adding Actin Polymerization Buffer 10X before analysis using a Synergy H1 plate reader (BioTek, VT, USA) in kinetic mode (one minute intervals), with an excitation wavelength of 360 nm and an emission wavelength of 407 nm. Results were normalized to actin polymerization alone and area under curves were compared between conditions.

Phylogenetic analysis of PALMD

A phylogenetic analysis of PALMD sequence was performed using the phylogeny platform (http://www.phylogeny.fr/)(Dereeper et al., 2008). PALMD sequences were downloaded from ENSEMBL (http://useast.ensembl.org/index.html) for Anolis carolinensis, Bos taurus, Canis lupus familiaris, Equus caballus, Gallus gallus, Macaca mulatta, Microcebus murinus, Mus musculus, Mustela putorius furo, Ornithorhynchus anatinus, Oryctolagus cuniculus, Pan troglodytes, Pongo abelii, Sarcophilus harrisii, Sus scrofa, Homo sapiens, Xenopus laevis and Xenopus tropicalis.

Statistical analysis

Continuous data were expressed as mean ± SEM, except when data are shown in violin plots, median and quartiles are indicated. Normality of distribution was tested with the Shapiro-Wilk test and data compared with Student *t*-test or Anova when two or more than two groups were compared respectively. Data with a non-normal distribution were compared between groups with non-parametric Wilcoxon-Mann-Whitney or Kruskal-Wallis test when two or more than two groups were compared respectively. *Post-hoc* Dunn multiple comparisons test were performed when the *P* value of the Kruskal-Wallis test was <0.05. Categorical data were expressed as percentage and compared with Fischer's exact test. A *P*-value < 0.05 was considered significant. Statistical analysis was performed with a commercially available software package Prism 8.

References

Brand, L.H., Kirchler, T., Hummel, S., Chaban, C., and Wanke, D. (2010). DPI-ELISA: a fast and versatile method to specify the binding of plant transcription factors to DNA in vitro. Plant Methods *6*, 25.

Chiu, T.-P., Rao, S., Mann, R.S., Honig, B., and Rohs, R. (2017). Genome-wide prediction of minor-groove electrostatic potential enables biophysical modeling of protein-DNA binding. Nucleic Acids Res. *45*, 12565–12576.

Dekker, J. (2006). The three "C" s of chromosome conformation capture: controls, controls, controls. Nat. Methods *3*, 17–21.

Dereeper, A., Guignon, V., Blanc, G., Audic, S., Buffet, S., Chevenet, F., Dufayard, J.-F., Guindon, S., Lefort, V., Lescot, M., et al. (2008). Phylogeny.fr: robust phylogenetic analysis for the non-specialist. Nucleic Acids Res. *36*, W465-469.

Hagège, H., Klous, P., Braem, C., Splinter, E., Dekker, J., Cathala, G., de Laat, W., and Forné, T. (2007). Quantitative analysis of chromosome conformation capture assays (3C-qPCR). Nat. Protoc. *2*, 1722–1733.

Jo, S., Vargyas, M., Vasko-Szedlar, J., Roux, B., and Im, W. (2008). PBEQ-Solver for online visualization of electrostatic potential of biomolecules. Nucleic Acids Res. *36*, W270–W275.

Kumar, S., Ambrosini, G., and Bucher, P. (2017). SNP2TFBS - a database of regulatory SNPs affecting predicted transcription factor binding site affinity. Nucleic Acids Res. *45*, D139–D144.

Langfelder, P., and Horvath, S. (2008). WGCNA: an R package for weighted correlation network analysis. BMC Bioinformatics *9*, 559.

McLean, C.Y., Bristor, D., Hiller, M., Clarke, S.L., Schaar, B.T., Lowe, C.B., Wenger, A.M., and Bejerano, G. (2010). GREAT improves functional interpretation of cis-regulatory regions. Nat. Biotechnol. *28*, 495–501.

Mumbach, M.R., Rubin, A.J., Flynn, R.A., Dai, C., Khavari, P.A., Greenleaf, W.J., and Chang, H.Y. (2016). HiChIP: efficient and sensitive analysis of protein-directed genome architecture. Nat. Methods *13*, 919–922.

Pettersen, E.F., Goddard, T.D., Huang, C.C., Couch, G.S., Greenblatt, D.M., Meng, E.C., and Ferrin, T.E. (2004). UCSF Chimera--a visualization system for exploratory research and analysis. J. Comput. Chem. *25*, 1605–1612.

Sagendorf, J.M., Berman, H.M., and Rohs, R. (2017). DNAproDB: an interactive tool for structural analysis of DNA-protein complexes. Nucleic Acids Res. *45*, W89–W97.

Servant, N., Varoquaux, N., Lajoie, B.R., Viara, E., Chen, C.-J., Vert, J.-P., Heard, E., Dekker, J., and Barillot, E. (2015). HiC-Pro: an optimized and flexible pipeline for Hi-C data processing. Genome Biol. *16*, 259.

Shashikant, T., Khor, J.M., and Ettensohn, C.A. (2018). Global analysis of primary mesenchyme cell cis-regulatory modules by chromatin accessibility profiling. BMC Genomics *19*, 206.

Thériault, S., Gaudreault, N., Lamontagne, M., Rosa, M., Boulanger, M.-C., Messika-Zeitoun, D., Clavel, M.-A., Capoulade, R., Dagenais, F., Pibarot, P., et al. (2018). A transcriptome-wide association study identifies PALMD as a susceptibility gene for calcific aortic valve stenosis. Nat. Commun. *9*, 988.

Tripathi, S., Pohl, M.O., Zhou, Y., Rodriguez-Frandsen, A., Wang, G., Stein, D.A., Moulton, H.M., DeJesus, P., Che, J., Mulder, L.C.F., et al. (2015). Meta- and Orthogonal Integration of Influenza "OMICs" Data Defines a Role for UBR4 in Virus Budding. Cell Host Microbe *18*, 723–735.

Wu, T., Mu, Y., Bogomolovas, J., Fang, X., Veevers, J., Nowak, R.B., Pappas, C.T., Gregorio, C.C., Evans, S.M., Fowler, V.M., et al. (2017). HSPB7 is indispensable for heart development by modulating actin filament assembly. Proc. Natl. Acad. Sci. *114*, 11956–11961.

Yang, L., Zhou, T., Dror, I., Mathelier, A., Wasserman, W.W., Gordân, R., and Rohs, R. (2014). TFBSshape: a motif database for DNA shape features of transcription factor binding sites. Nucleic Acids Res. *42*, D148-155.